A Universal Force Field for Materials, Periodic GFN-FF: Implementation and Examination

Julian D. Gale, Luc M. LeBlanc, Peter R. Spackman, Alessandro Silvestri, Paolo Raiteri*

Curtin Institute for Computation, School of Molecular and Life Sciences, Curtin University, PO Box U1987, Perth, WA 6845, Australia

ABSTRACT

In this study, the adaption of the recently published molecular GFN-FF force field for periodic boundary conditions (pGFN-FF) is described through the use of neighbor lists, combined with appropriate charge sums to handle any dimensionality from 1-D polymers through 2-D surfaces through to 3-D solids. Numerical integration over the Brillouin zone for the calculation of π bond orders of periodic fragments is also included. Aside from adapting the GFN-FF method to handle periodicity, improvements to the method are proposed in regard to the calculation of topological charges through the inclusion of a screened Coulomb term that leads to more physical charges and avoids a number of pathological cases. Short-range damping of three-body dispersion is also included to avoid collapse of some structures. Analytic second derivatives are also formulated with respect to both Cartesian and strain variables, including pre-screening of terms to accelerate the dispersion/coordination number contribution to the

Hessian. The modified pGFN-FF scheme is then applied to a wide range of different materials in order to examine how well this universal model performs.

1. INTRODUCTION

Force field methods are a valuable tool for the rapid calculation of material structure and properties via optimization and lattice dynamics. Whether used as a precursor to more accurate and computationally demanding first principles techniques, or standalone, they offer a means to explore the influence of different interaction models on the results, thereby offering physical insight. Unfortunately, the initial creation of a force field model for a new material via fitting can be a long and involved process that negates the benefit of the speed of the calculations that are ultimately performed. Hence a key objective of the simulation field is to find models that have as broad applicability as possible, with the idea of a universal force field covering all possible systems representing the perfect scenario that eliminates the need for specific parameterization.

Despite the appeal of a universal force field for all materials, there have been relatively few published models that aim for broad coverage with minimal or, ideally, no user intervention. One of the first attempts was the DREIDING force field[1] that offered coverage of organic molecules and a number of primarily main group elements, with the stated objective that it would be simple to add further elements and their corresponding parameters. In a similar vein, other force fields offering parameters for a mix of organics and inorganics also began to appear, such as CFF91.[2] Shortly afterwards came the Universal Force Field (UFF),[3] which offered, for the first time, full coverage of the periodic table as it then stood. As with any generic force field, it is unlikely to be the optimal model for any given specific system and so UFF has been subsequently refined for particular materials such as metal-organic frameworks.[4] There have

also been modifications proposed, such as XUFF,[5] to address the inconsistency between geometry-dependent charges generated via the QEq model[6] for electronegativity equalization and the UFF electrostatics that use fixed (or no) charges with a pure Coulomb potential.

Given the rapid advances made in the space of a few years at the start of the 1990s, it is surprising that further progress in the development of universal force fields has been a long time coming. While the recent surge in the use of machine-learning approaches could be viewed as use of a universal force field,[7] insofar as the representation is largely agnostic to the details of the material being studied, such methods place even greater demands on the parameterization phase than traditional, physically-motivated force fields. Recently, Spicher and Grimme have proposed a new general force field model, GFN-FF,[8] that is capable of handling compounds of all elements up to and including radon (atomic number 86). Results were presented indicating that GFN-FF is capable of successfully modelling a wide range of systems from biomolecules through to inorganic materials. To date, this new force field has only been available in the XTB code[9] and was only implemented for finite systems (i.e., clusters or molecules). The objective of this work is to first describe the extension of the GFN-FF approach to periodic boundary conditions, as well as the implementation of analytic second derivatives to supplement the gradients that were previously available. This includes the addition of derivatives with respect to strain to augment those for atomic coordinates.

During the implementation of periodicity it became apparent that there were a number of opportunities for improvement of some aspects of the methodology, which has led to the proposal to adopt a slightly modified form better suited to condensed phases, which we denote as pGFN-FF. Having implemented this method, we perform an examination of how successful (p)GFN-FF is for the prediction of geometries, energies and properties for several important classes of solid-state material.

2. METHODS

The GFN-FF method is designed to provide a general force field that is fully automated for all atoms, thereby removing some of the difficulties of other approaches where (often manual) assignment of atom types is required. The main components of the energy are electrostatics, dispersion, hydrogen-bonding and covalent terms covering bond stretching, angle bending, torsions and out of plane distortions. A full description of the method can be found in the original manuscript,[8] plus the source code of the implementation in XTB,[9] and so the focus here will be primarily on the features that require modification for implementation within periodic boundary conditions.

2.1. Periodic boundary conditions.

The primary objective of this work is to allow GFN-FF to be applied to solids, surfaces and polymers in addition to molecules. Therefore, the main change is that configurations now include not just the atomic coordinates, but also a general number of lattice vectors up to and including three. This means a unit cell (3D), surface vectors (2D) or a single repeat direction (1D) can be specified alongside an appropriate combination of Cartesian and/or fractional coordinates appropriate to the dimensionality.

In the original XTB implementation of GFN-FF the distance between a pair of atoms was pre-computed for each configuration and stored in a lower-half triangular matrix. When working within general periodic boundary conditions, without the pre-condition of the minimum image convention, there will now be potentially multiple interactions per pair of atoms due to the translational images. To handle this, as well as the presence of general boundary conditions, our implementation of GFN-FF uses a neighbor list for each atom that stores each image that lies within the maximum cut-off distance applicable to that atom. This has several advantages. Firstly, the nature of the boundary conditions being used is confined to the construction of the neighbor list and is largely hidden during the calculation of the GFN-

FF energy. Secondly, in the limit of spatially large systems, the memory required to store the interactions scales linearly with the number of atoms, rather than quadratically. The present implementation also has the option to choose between building the neighbor list via looping over all images of pairs of atoms or using a domain-decomposition algorithm which is more efficient for large systems.

A further consequence of periodicity is that optimization with respect to the lattice vector(s) is often required, as well as the calculation of properties that depend on the curvature of the energy surface with respect to the repeat unit, such as elastic constants and bulk moduli. The variation of lattice vectors, $\boldsymbol{R}$, is accomplished through the application of the Voight strain matrix, $\boldsymbol{\varepsilon}$, to a reference set of lattice vectors, $\boldsymbol{R_0}$:

$$\boldsymbol{R} = \boldsymbol{\varepsilon R_0}$$

$$\boldsymbol{\varepsilon} = \begin{pmatrix} 1+\varepsilon_1 & \frac{1}{2}\varepsilon_6 & \frac{1}{2}\varepsilon_5 \\ \frac{1}{2}\varepsilon_6 & 1+\varepsilon_2 & \frac{1}{2}\varepsilon_4 \\ \frac{1}{2}\varepsilon_5 & \frac{1}{2}\varepsilon_4 & 1+\varepsilon_3 \end{pmatrix}$$

Here the matrix is written for the 3-D periodic case where there are 6 unique components of the tensor, while for 2-D and 1-D boundary conditions this reduces to 3 and 1 components, respectively. Based on this equation it is straightforward to compute the derivatives of the energy with respect to the strain alongside the Cartesian derivatives of the coordinates, α:

$$\left(\frac{\partial U}{\partial \alpha}\right) = \left(\frac{1}{r}\frac{\partial U}{\partial r}\right)\left(\frac{1}{2}\frac{\partial r^2}{\partial \alpha}\right) = \left(\frac{1}{r}\frac{\partial U}{\partial r}\right)\alpha$$

$$\left(\frac{\partial U}{\partial \varepsilon}\right) = \left(\frac{1}{r}\frac{\partial U}{\partial r}\right)\left(\frac{1}{2}\frac{\partial r^2}{\partial \varepsilon}\right)$$

Note that here the conventional approach is taken of using the current lattice vectors as the reference set, such that the strain derivatives are computed in the limit of the strains being infinitesimal, in order to simplify the result expressions for the derivative of the vector norm

squared with respect to strain. Full expressions for the first and second derivatives using this approach can be found elsewhere.[10]

2.2. Electrostatics

In GFN-FF, the electrostatic energy is computed as a pairwise sum over the interaction between atom-centered point charges. Here, the charges are geometry-dependent and determined by electronegativity equalization.[11] In practice, there are actually two sets of atomic charges that are utilized in the method; the first set is determined based on an idealized topological configuration and is used for the charge-dependence of force field parameters, while the second set is computed for the actual geometry to determine the electrostatic energy. This dual charge model eliminates the need to compute the extra derivatives of force field parameters arising due to the charge-dependence, as the topological charges are independent of the actual configuration, provided the bonding pattern remains the same. Focusing on the charge-determination for the actual geometry of a system with N atoms, the expression for the energy is given by;

$$U_q = \sum_{i=1}^{N} \left[(\chi_i + \kappa_i c_i) q_i + \frac{1}{2}\left(\eta_i + \frac{2\gamma_{ii}}{\sqrt{\pi}}\right) q_i^2 + \frac{1}{2}{\sum_{j=1}^{N}}' q_i q_j \frac{erf(\gamma_{ij} r_{ij})}{r_{ij}} \right]$$

where q_i is the charge on atom i, r_{ij} is the distance between atoms i and j, and the pairwise sum over Coulomb interactions excludes the case of $i = j$ when they are in the same unit cell. There are two key points to highlight regarding this equation. Firstly, the electronegativity of each atom has a contribution that depends on the coordination number (expressed via a square-rooted log function as c_i, scaled by an atom-specific factor, κ_i) in addition to the standard elemental value, χ_i, while the hardness is given by η_i. Secondly, the Coulomb interaction between two atoms is damped at short-range through the inclusion of the error function with a decay factor, γ_{ij}, that depends on the atomic radii of the two atoms involved.

Arguably the most significant change required between finite systems and periodic boundary conditions is the need to handle the conditional, or slow, convergence of the electrostatic energy sums. As is standard, we choose to handle this in 3-D and 2-D through partial transformation into reciprocal space of the Coulomb terms as proposed in the Ewald[12] and Parry[13] sums, respectively:

$$U^{3D} = U^{3D}_{recip} + U_{real} + U_{self}$$

$$U^{2D} = U^{2D}_{recip} + U^{2D}_{z} + U_{real} + U_{self}$$

$$U^{3D}_{recip} = \frac{1}{2}\frac{4\pi}{V}\sum_{i=1}^{N}\sum_{j=1}^{N}\sum_{G} q_i q_j exp\left(i\boldsymbol{G}\boldsymbol{r}_{ij}\right)\frac{exp(-G^2/4\eta)}{G^2}$$

$$U^{2D}_{recip} = \frac{1}{2}\frac{\pi}{A}\sum_{i=1}^{N}\sum_{j=1}^{N}\sum_{G} q_i q_j \frac{exp\left(i\boldsymbol{G}\boldsymbol{r}_{ij}\right)}{|G|}\left[exp\left(|G|z_{ij}\right)erfc\left(\frac{|G|}{2\eta^{1/2}} + \eta^{\frac{1}{2}}z_{ij}\right)\right.$$

$$\left. + exp\left(-|G|z_{ij}\right)erfc\left(\frac{|G|}{2\eta^{1/2}} - \eta^{\frac{1}{2}}z_{ij}\right)\right]$$

$$U^{2D}_{z} = \frac{1}{2}\frac{2\pi}{A}\sum_{i=1}^{N}\sum_{j=1}^{N} q_i q_j \left[z_{ij}erf\left(\eta^{\frac{1}{2}}z_{ij}\right) + \frac{exp\left(-\eta z_{ij}^2\right)}{(\pi\eta)^{1/2}}\right]$$

$$U_{real} = \frac{1}{2}\sum_{i=1}^{N}\sum_{j=1}^{N} q_i q_j \frac{erfc\left(\eta^{1/2}r_{ij}\right)}{r_{ij}}$$

$$U_{self} = -\sum_{i=1}^{N} q_i^2 \left(\frac{\eta}{\pi}\right)^{\frac{1}{2}}$$

Here, V and A are the volume and area of a 3-D and 2-D repeating system, respectively. The distance z in 2-D represents the height normal to the surface plane. The parameter η determines the balance between real and reciprocal space, and is chosen to minimize the computational work in summing over real space vectors, $\boldsymbol{r}$, and reciprocal lattice vectors, $\boldsymbol{G}$, out to the cut-off values that are selected to converge the energy to a given number of significant figures (by

default 12 in the present work). It should be noted that the above sums again exclude the real space terms where $r_{ii} = 0$, as well as the reciprocal space case of $G = 0$.

In the case of 1-D polymer boundary conditions, the Coulomb sum is convergent, but slow to do so. Therefore, we utilize the method proposed by Saunders *et al*[14] to accelerate the convergence of the electrostatics for this case. Because, as noted above, GFN-FF multiplies the Coulomb term by the error function, it is necessary to compute an additional term in real space that corrects for the difference between the standard lattice sums for 1/r and this modified form. The cut-off radius for this correction is set by default to four times the largest atomic radius that enters into the coefficient for the error function. This leads to an error of the order of 10^{-8} in the numerator, but the overall error is lower than this due to division by the distance and the cancellation of differences when multiplied by charge products summed across the lattice for a charge neutral system.

Having computed the Coulomb matrix elements between atoms in the system, then it is necessary to solve the electronegativity equalization equations in order to determine the charges for which U_q is at a minimum, subject to the charge constraints on fragments, from which the final electrostatic energy can be calculated. This can be written as;

$$\boldsymbol{A}\,\boldsymbol{q} = \boldsymbol{b}$$

where $\boldsymbol{A}$ is the matrix of all terms that depend linearly on the atomic charges, which are contained in the vector, $\boldsymbol{q}$, while the final vector, $\boldsymbol{b}$, contains the corresponding terms that are charge-independent, such as the electronegativities and any external potential. In the original implementation of GFN-FF the solution of this equation is performed by factorization and solution of the electronegativity problem to avoid explicit inversion of the matrix. Although not connected with periodicity, we have added an alternative approach here which is to exploit the variational nature of the problem and minimize the charges using conjugate gradients under the total charge constraint for each fragment, as used previously in GULP for other

electronegativity equalization approaches and also by others.[15] For large systems where the charges vary slowly between energy evaluations (as is typically the case during molecular dynamics or a nearly converged optimization) the use of minimization can be advantageous since it has a lower scaling with problem size and exploits the fact that a good approximation to the final solution is already known.

In the iterative minimization of the charges described above, it is useful to precondition the conjugate gradients algorithm to accelerate the rate of convergence:

$$(\boldsymbol{PA})\boldsymbol{q} = (\boldsymbol{Pb})$$

where the preconditioning matrix, $\boldsymbol{P}$, is used to approximate $\boldsymbol{A}^{-1}$. By default, the algorithm uses the reciprocal of the diagonal elements of $\boldsymbol{A}$ as a simple approximation to the full inverse, which is reasonable if the system is diagonally dominant. This appears to work reasonably well for conventional electronegativity equalization, in that after an initially large number of iterations, and assuming the charge vector is initialized to zero, then the convergence rapidly reduces to fewer iterations for a sequence of relatively similar geometries (such as during a molecular dynamics trajectory). In the case of GFN-FF, it was found that the number of iterations per step may not always decay as quickly, which may be due to the fragment-based charge constraints rather than a single global one. Hence, we have also implemented an option to compute the exact inverse of $\boldsymbol{A}$ for the first step, which can then be used as a preconditioner for subsequent iterative solutions. Here, the initial overhead of the matrix solve is compensated if, for example, molecular dynamics is subsequently performed. In the case of a cubic box containing 520 water molecules, the use of the full inverse preconditioner reduces the number of iterations for the conjugate gradients solver from of order 200 per step to less than 10. Given the algorithm already includes several dense matrix-vector multiplies, the extra cost of full preconditioning does not dramatically increase the overall computational demands. This

scheme could be further improved by using an updating scheme such as DFP or BFGS to allow the preconditioning matrix to evolve during the simulation.

When computing only first derivatives, the variational nature of the charges means that the Hellmann-Feynman theorem applies and so there is no need to explicitly calculate the derivatives of the charges with respect to the coordinates or strain. However, the implementation of analytic second derivatives necessitates the determination of these quantities. In this case, the charge first derivatives with respect to a coordinate α, which could be a Cartesian component or strain, are given by:

$$\left(\frac{\partial \boldsymbol{q}}{\partial \alpha}\right) = -\boldsymbol{A}^{-1}\left(\frac{\partial \boldsymbol{A}}{\partial \alpha}\right)\boldsymbol{A}^{-1}\boldsymbol{b} + \boldsymbol{A}^{-1}\left(\frac{\partial \boldsymbol{b}}{\partial \alpha}\right)$$

Since this requires the inverse of the matrix used in electronegativity equalization, the explicit inverse is computed and temporarily stored for second derivative evaluations.

When computing the second derivative matrix for GFN-FF the charge first derivatives are included via the following expression:

$$\left(\frac{\partial^2 U}{\partial \alpha_k \partial \beta_l}\right) = \left(\frac{\partial^2 U}{\partial \alpha_k \partial \beta_l}\right)_q + \sum_{i=1}^{N}\sum_{j=1}^{N}\left(\frac{\partial^2 U}{\partial q_i \partial q_j}\right)_r \left(\frac{\partial q_i}{\partial \alpha_k}\right)\left(\frac{\partial q_j}{\partial \beta_l}\right)$$
$$+ \sum_{i=1}^{N}\left\{\left(\frac{\partial^2 U}{\partial q_i \partial \alpha_k}\right)\left(\frac{\partial q_i}{\partial \beta_l}\right) + \left(\frac{\partial^2 U}{\partial q_i \partial \beta_l}\right)\left(\frac{\partial q_i}{\partial \alpha_k}\right)\right\}$$

Here, the first term on the right-hand side is the conventional second derivative for fixed charges, the second term represents the partial second derivative of the energy with respect to both charges for pairwise interactions, while the final terms are the mixed partial derivatives of the gradients with respect to charge. The optimization variables, α and β, are the coordinates for atoms k and l in the system, with corresponding expressions for the strain and mixed derivatives. The key point to highlight in this equation is that the evaluation of the second term as written scales as N^2, but since the number of second derivative matrix elements also has the same scaling, the cost of evaluating this contribution can potentially increase to N^4. If

implemented in this form, then this rapidly becomes the computational bottleneck for the method, as it is the only operation that exceeds the cubic scaling of other operations such as matrix inversion or diagonalization. Therefore, we compute the second term via two successive operations involving multiplication and summing over one charge derivative term, with storage of the intermediate matrix, which reduces the scaling to N^3. Furthermore, rather than adding the terms "on the fly" as the partial second derivatives with respect to two charges are computed, these terms are stored as a matrix with the addition of this term in the charge derivatives being added at the end of the Coulomb sum. For solids, this reduces the cost by a factor of two, if real and reciprocal space terms are determined separately, for the overhead of a matrix that is 9 times smaller than the Hessian or dynamical matrix.

Although GFN-FF is designed to be a fully automated universal force field, there are choices that can be made that significantly influence the outcome of a calculation: One of these is the total charge of the fragments involved. While the default is to constrain all fragments to be neutral, this can lead to problems for some systems where this goes against chemical intuition. For example, there are a range of metal-organic framework structures that have perchlorate (ClO_4^-) as a counter ion within the structure, while numerous minerals have molecular anions within their structure, such as carbonate and sulfate. If these fragments are allowed to remain as neutral entities, then the optimizations can fail as the coordination of the species is not appropriate to their charge. In the current implementation, initial charges can be input as part of the structure and these decide the net fragment charge. Hence, setting a charge on Cl to -1 for perchlorate, with zero for the corresponding oxygens, implies that the fragment charge will be constrained to -1. The influence of setting fragment charges during the initialization of the force field calculation will be considered later in discussion of the results for minerals containing molecular anions.

During the analysis of results for some materials, such as perovskites as discussed below, it became apparent that the fragments created were not always those that would be expected based on the bonding topology of the system. This is because, in the original algorithm, the fragments are determined using the full neighbor list, rather than just the reduced bonding neighbor list. In order to provide a more intuitive connection between bonding and fragments, an option has been added to allow fragments to be determined strictly in accordance with the bonding topology.

2.3. Topological charges

In addition to the charges that are computed on the fly during the actual energy evaluation, there are also charges that are used during the determination of force field parameters. Here the distances for the Coulomb interactions between atoms are set based on the bonding connectivity with all distances that are not explicitly defined for nearest-neighbors being set to a constant value. If this constant distance is large, then the Coulomb interaction naturally tends to zero. In the original implementation of GFN-FF this large limiting distance was intended to be very large (10^{+12} a.u.) but in practice ended up being set to 13 a.u.. For molecules, the difference between a small, but finite, value and an infinitesimally small value can often be less critical because the charges tend to be small and the range of interaction limited. For periodic systems, it is necessary for the Coulomb interaction to go to zero with increasing distance since there are, in principle, an infinite number of interactions unless a further cut-off is applied. Hence, in this work, all distances that are not set as part of the topological neighbor list are either excluded or set to a very large value, which amounts to the same thing in practice.

A further difference relative to the original molecular implementation is how to handle the potential existence of multiple interactions between a given pair of atoms due to periodic images. This is achieved by building a topological neighbor list for all atoms, which is initialized to be equal to the bonding neighbor list, except that the distance between the atoms

is given by the sum of their atomic radii. Subsequently, iterations are performed over successive shells to search for new topological connections. Here, the search is over neighbors of a central atom that were added in the previous iteration and a second neighbor of the same atom. If the sum of the distances to the common central atom is less than the current distance between the pair, or if the pair doesn't yet exist in the neighbor list, then the distance for the pair is set to the lower value or the pair added to the neighbor list with this value, respectively. All of this is subject to a maximum topological distance cut-off (which has a default value of 12 a.u.). When checking for matches in the topological neighbor list, the vector between pairs of atoms is used rather than just the atom numbers in order to allow for multiple images of the same atom occurring. It should be noted that once the set of topological distances is complete then a scaling factor (1.175) is applied to all values, as per the original implementation.

Tests on the convergence of the topological neighbor list suggest that 4 iterations, on top of the original bonding list, is sufficient for most systems to find all neighbors that lie within the cut-off distance. An interesting pathological case was found for the mineral gibbsite ($Al(OH)_3$) where the Al is found to have 9-fold coordination within the GFN-FF criteria, due to binding 6 hydroxyl groups and having bonds to the 3 adjacent Al atoms within the same layer. On the second pass through the topology determination, there was found to be an explosion in the number of neighbors resulting in a dramatic slowdown of the method. This was found to be caused by the initial set of topological charges in the first iteration being extreme and unphysical (i.e., some atoms had charges close to -5). The atomic radii used to define the bonding cut-off depend linearly on the charge according to;

$$R_{ij} = R_{ij}^{CN} - f_i^q q_i - f_j^q q_j$$

where R_{ij}^{CN} is the sum of the radii for a pair of atoms i and j corrected for the coordination number, and f_i^q and f_j^q are constants with the value 0.23 or 0.46 for non-metals and metals, respectively. Given this, if any charge becomes highly negative, then the bonding cut-off, and

thus also the number of neighbors, can dramatically increase. By including a reduced number of neighboring shells (for example 2) in the first iteration of the parameter set in GFN-FF, it was found that this problem could be avoided and convergence to the correct parameters was then achieved in a stable manner during subsequent iterations with the full set of topological neighbors.

A further problem with unphysical charges when using the original algorithm was encountered for a number of systems, especially for more ionic combinations of elements. One such example was SrO in the rock salt structure when the lattice parameter is close to the experimental value. Here the charges again became unphysically large within the original algorithm. This led to a failure in the determination of the short-range repulsion where the presence of large negative charges resulted in the expression for an atom-centered parameter becoming negative and the pairwise interactions, which are given by the square root of the product for a pair of atoms, becoming complex in some cases. This exception is now trapped within our implementation, though it raises the question of what causes such behavior to occur and how to avoid it? Analysis of several of these cases also revealed that often it was the metal ions that were carrying the excessively negative charge and more broadly, even when the charges were small, it was quite common for the polarity to be the opposite of what might be anticipated for the compound.

The cause of the above problems in an extended system is actually the use of a cut-off radius for the Coulomb interactions during the charge equalization scheme. Just as the need for an Ewald sum is readily appreciated for periodic systems, due to the conditional convergence of the charge sum, the same situation applies to the topological charges for any system where the dimensions exceed the cut-off radius, regardless of periodicity. Depending on where the cut-off truncates the number of interaction shells of neighbors, this can lead to large fluctuations in the net charge experienced by a given atom with unphysical charges being the result. One

solution to this would be, in principle, to introduce periodic charge sums as discussed for the real charges of the system. However, this is problematic for the topological interactions since there is no explicitly specified periodic lattice from which to define the reciprocal space contribution. To stay within the spirit of the original approach of a finite number of interaction shells with a set of topological distances it is therefore proposed to use the so-called Wolf sum[16] technique. The advantage of this method is that the Coulomb interactions are evaluated purely in real space and so the correction does not require *a priori* knowledge of a lattice, plus the method can be applied even for non-periodic systems. In effect, this means that the Coulomb potential for the topological charges is scaled by a complementary error function and shifted such that the interaction goes to zero at the cut-off radius, R_c:

$$V_{Coulomb}^{topo} = erf(\gamma_{ij} r_{ij}) \left[\frac{erfc(\eta_W r_{ij})}{r_{ij}} - \frac{erfc(\eta_W R_c)}{R_c} \right]$$

This form of interaction introduces one new parameter that controls the rate of decay of the Coulomb interactions, η_W, which can be chosen to balance the requirement to maintain the original unscreened interactions at short-range while causing the terms to decay sufficiently toward the cut-off radius. In the present work a value of $\eta_W = 0.2$ Å^{-1} was used.

We note that there have been improvements to the Wolf sum suggested that address the smoothness and consistency of the energy and forces at the cut-off radius.[17] However, here the original summation suffices since only the site potentials and energy are being computed. While results will be presented later to demonstrate the effect of the use of a Wolf sum to ensure convergent behavior based on a screened potential, it can be noted at this stage that this resolves the problem of excessive charges for all cases explored to date. Furthermore, it is also found to yield charges that are more in line with physical intuition, such as metal oxides where the metal is positive and the oxygen negative, since the Coulomb interactions are weighted more toward the first shell of neighbors.

2.4. π systems

As part of the parameter determination, GFN-FF iteratively performs Hückel calculations for any conjugated systems to determine the hybridization state and bond orders for selected elements. Built into this is a check as to whether the occupation of the π system is reasonable based on the estimated number of π electrons. When an issue is detected then the total number of electrons is reduced by 1 and the process repeated. Given that conjugated systems can formally carry either an excess negative or positive charge, an option has been added to allow the number of electrons to be increased by 1 rather than decreased. Since the majority of cases where this will occur are for molecular anions, our implementation uses the sum of the atomic charges for the atoms in the π system to determine whether the number of electrons is incremented or decreased for negatively or positively charged systems, respectively.

A further consideration when performing the Hückel calculation is that, for periodic boundary conditions, there may be a continuous conjugated system along one or more dimensions of the system. For example, graphene is such a case with a 2D periodic π system. This means that the Hückel equations must also be integrated across the Brillouin zone when determining the Fermi level for the system and π bond orders. As is conventional, this integral can be approximated by a sum over discrete points in reciprocal space, most commonly using a Monkhorst-Pack mesh[18]. Thus, we adopt a similar approach here and create a grid of k points at which the Hückel equations are solved. To simplify this process, the reciprocal space grid can automatically be generated in any number of dimensions using a single control parameter, k_{max}, which is the maximum allowed spacing between any two adjacent grid points. Note that the number of grid points is approximately halved due to time reversal symmetry. Convergence is then just a matter of decreasing the value until the energy of the system no longer changes to within an acceptable tolerance. Based on graphene, a value of 0.04 $Å^{-1}$ for k_{max} appears to be sufficient to achieve convergence, and so this is taken as the default value.

Having defined the grid of k points, the Hückel equations can be formulated as;

$$H_{ij}(\boldsymbol{k}) = \delta_{ij}\left[H_i^{on} + \lambda_{Hp3}q_i - \lambda_{Hpf}(n_i^{\pi} - 1)\right] - \left(1 - \delta_{ij}\right)\left[t_1^H\left(1 - t_2^H\left(\frac{2}{3} - P_{ij}^{\pi}\right)\right)\right] exp\left(i\boldsymbol{k}\boldsymbol{r}_{ij}\right)$$

$$t_1^H = \sqrt{H_i^{off} H_j^{off}} - \lambda_{Hpr} r_{ij}$$

$$t_2^H = \lambda_{Hpi} h_{triple}^i h_{triple}^j$$

where λ_{Hp3}, λ_{Hpf}, λ_{Hpi} and λ_{Hpr} are constants for GFN-FF with the values -0.24, 0.53, 0.7 and 10^{-9}, respectively, H_i^{on} is the on-diagonal self-term for the given element, H_i^{off} and H_j^{off} are the off-diagonal parameters for the elements corresponding to *i* and *j*, and n_i^{π} is the number of π electrons of atom *i*. The terms h_{triple}^i and h_{triple}^j are either 1.45 or 1.0 depending on whether the atoms are involved in a triple bond or not, respectively. Numerical values for the Hamiltonian are all given in atomic units. The matrix element P_{ij}^{π} is from the density matrix from the previous iteration and is initialized to 2/3 for the first cycle. Subsequently, it is computed from the eigenvectors of the matrices $H(\boldsymbol{k})$, $\psi^{\pi}(\boldsymbol{k})$, according to;

$$P_{ij}^{\pi} = \sum_k \sum_n \psi_{in}^{\pi *}(\boldsymbol{k}) o_n(\boldsymbol{k}) \psi_{jn}^{\pi}(\boldsymbol{k})\, exp\left(i\boldsymbol{k}\boldsymbol{r}_{ij}\right)$$

where $o_n(\boldsymbol{k})$ represents the occupancy of the *n*th eigenstate at the given point in reciprocal space, as determined by the Fermi level and electronic temperature. It should be noted that the GFN-FF formalism scales the eigenvalues by a factor of 0.1 to reduce the gap.

Although the above sum over k points and the need for complex arithmetic increases the cost of determining the π bond orders significantly, this still typically represents an insignificant overhead as it is only required to be performed once at the start of each new material to set the parameters. It is also substantially more efficient than using the alternative of a supercell approach to remove the size dependence of the parameters, since this increases the cost of all

parts of the calculation. Since it is possible to use the neighbor list to automatically detect which π fragments are periodic and which are finite (even though they might be part of a periodic material), the extra cost can be minimized by only using the gamma point for non-periodic π systems.

Once the π bond orders, P_{ij}^{π}, are determined according to the above procedure, the value is used to compute a correction to the equilibrium bonding distance between pairs of atoms, R_{ij}^{0}, according to the formula:

$$R_{ij}^{0} = R_{ij}^{0\prime} + 0.34\left(0.37 - P_{ij}^{\pi}\right)$$

In the original implementation of GFN-FF, the decision as to whether this correction should be applied is based on whether the π bond order is greater than zero. Unfortunately, this was found to be problematic since any rounding error in the calculation of the π bond order could lead to a small, but not exactly zero value, and since the π correction to bonding does not increase linearly with the π bond order then this can lead to a semi-random change in the parameters. For example, when running the mineral system calcite ($CaCO_3$), where the carbonate groups sit on three-fold axes of rotation such that all bonds in the carbonate group are symmetry equivalent, symmetry breaking was found to occur in some groups. This was because the π bond order was 10^{-16} rather than exactly zero to double precision. To avoid such problems, a small, but finite tolerance (10^{-8}) has been used to check the need for the π bonding correction.

2.5. Cut-offs

There are several interaction terms in GFN-FF that are evaluated with cut-offs that are controlled via a single accuracy parameter. Specifically, these limit the calculation of the dispersion, long-range repulsion, coordination number, and hydrogen bonding interactions. In the current implementation we have made two changes to this scheme. Firstly, a separate

accuracy parameter has been introduced for each term so that the convergence of each term can be controlled separately, if desired. Secondly, instead of having a hard cut-off, which can potentially lead to discontinuities and problems with the smoothness of the energy surface (e.g., when computing numerical derivatives from finite differences), a taper function, t, has been applied over a specified range from r_{min} to r_{max}. Here we use the MDF form of taper[19]:

$$x = \frac{(r - r_{min})}{(r_{max} - r_{min})}$$

$$t(x) = (1 - x)^3(1 + 3x + 6x^2)$$

This taper function ensures smooth transitions and consistent derivatives up to the order required for the present work. By default, the taper function is applied to go to zero over the final 5% of the interaction range as determined by the accuracy parameter(s).

2.6. Dispersion

In GFN-FF, the dispersion interactions are computed based on a modified form of the Grimme D4 scheme[20] that utilizes C_6 and C_8 terms. Based on the default accuracy, this term is evaluated with a hard pairwise cut-off distance of 50 a.u.. For molecules, this is not a particular issue. However, for dense solids the long-range cut-off can become a small, but noticeable, cost in the calculation. Where the cost becomes far more problematic is during the evaluation of the derivatives of this term, especially to second order. This is because the dispersion interaction depends not only on the distance between a pair of atoms, but also the coordination number of each atom. Therefore, while the energy is a pairwise sum, this becomes a double summation for forces and a triple sum for second derivatives. Ultimately, this can mean that for a Hessian evaluation the dispersion term becomes the dominant term in the computational cost and for high coordination numbers can increase the time by at least two orders of magnitude. Analysis of the second derivative contributions show that the majority of coordination number derivative terms are negligibly small. This is exploited by introducing a

drop tolerance, t_{drop}, for these terms such that the cost is dramatically reduced often with minimal effect on the Hessian matrix. Illustrative examples of the reduction in computational cost as a function of drop tolerance can be found in Table S1. Note that the drop tolerance is only used for the second derivatives and so, during optimization, there is no loss in precision for the converged final energy of the system. An example of how this is applied is given below:

$$\left(\frac{\partial^2 U\left(d, ln(c)\right)}{\partial r^2}\right)_d$$
$$= \left(\frac{\partial U}{\partial ln(c)}\right)\left(\frac{\partial ln(c)}{\partial c}\right)\left(\frac{\partial^2 c}{\partial r^2}\right)$$
$$+ \left[\left(\frac{\partial U}{\partial ln(c)}\right)\left(\frac{\partial^2 ln(c)}{\partial c^2}\right) + \left(\frac{\partial^2 U}{\partial ln(c)^2}\right)\left(\frac{\partial ln(c)}{\partial c}\right)^2\right]\left(\frac{\partial c}{\partial r}\right)^2$$

Here $U\left(d, ln(c)\right)$ is an energy term that depends on a distance, d (or potentially a set of distances), as well as one or more logarithms of coordination numbers, c. The above expression gives the partial second derivative with respect to an interatomic distance that contributes to one of the coordination numbers. If this term is below the drop tolerance, then the contribution is neglected. While strictly speaking the end result is, for example, the Cartesian second derivative contribution from this term, and so the magnitude of the derivatives of the distance with respect to the Cartesian components should be allowed for. However, screening each term at this level would create a much greater computational overhead, thereby reducing the benefit. Given that the missing terms are dependent on the magnitude of r, as is the term under consideration, then this neglect does not cause any significant contributions to be lost.

In the case of the dispersion energy, the drop tolerance is applied to all coordination number second derivatives if

$$\left(\frac{\partial^2 U}{\partial ln(c)^2}\right) < t_{drop}$$

in order to accelerate the Hessian calculation.

2.7. Bonded three-body dispersion

The GFN-FF formalism also includes the Axilrod-Teller-Muto (ATM) three-body dispersion contribution:

$$U_{3body} = \sum_{i,j,k} C_9^{ijk} \frac{\left(3cos\theta_{jik}cos\theta_{ijk}cos\theta_{ikj} + 1\right)}{r_{ij}^3 r_{ik}^3 r_{jk}^3}$$

Here, the dispersion coefficient, C_9^{ijk}, depends on the atomic topological charges and scaled nuclear charges of the three participating atoms, i, j, k. What is unique about the inclusion of this term is that it is only computed within a set of atoms where two are connected via three covalent bonds and the remaining atom is bonded to one of the others.

For optimizations of some systems, such as halides of Cs and Rb for example, the three-body dispersion term was found to be problematic. This is because the term becomes asymptotic to minus infinity at small distances, and so occasionally this dominates the short-range contribution from the repulsion, as can occur for the two-body Buckingham potential where the C_6 term is not damped. In the case of CsCl in the B2 structure, only a small barrier exists between the physically sensible minimum and a basin that leads to implosion of the structure and so there was a risk of the optimizer overstepping the barrier during the line search.

The solution to the above problem is to introduce damping for the three-body dispersion, as is applied to the two-body terms. However, there is no universally agreed functional form that this damping should take, as discussed by Otero-de-la-Roza and Johnson.[21] Here we have implemented the scheme A approach suggested by Proynov *et al*.[22] which introduces a constant for each distance separately in the spirit of Becke-Johnson damping:[23]

$$U_{3body} = \sum_{i,j,k} C_9^{ijk} \frac{\left(3cos\theta_{jik}cos\theta_{ijk}cos\theta_{ikj} + 1\right)}{\left(r_{0,ij}^3 + r_{ij}^3\right)\left(r_{0,ik}^3 + r_{ik}^3\right)\left(r_{0,jk}^3 + r_{jk}^3\right)}$$

The pairwise radial constants, r_0, that control the damping are determined following the protocol proposed for two-body dispersion[24] starting from the same radial values, r_c (since these are already defined within the GFN-FF method), via a linear relationship:

$$r_0 = \alpha_1 r_c + \alpha_2$$

While the values of the two coefficients, α_1 and α_2, could be considered as free parameters to be optimized separately for three-body dispersion, there is a lack of data for the ATM term evaluated within covalently-connected triples in the way applied here. Hence, we have taken the values of $\alpha_1 = 0.58$ and $\alpha_2 = 4.80$ a.u. as used already for the two-body dispersion damping in GFN-FF.

2.8. Hydrogen and halogen bonding

The search for hydrogen and/or halogen bonds used here largely follows the same approach as the original method, except for allowing for periodic images via the use of a neighbor list containing all distances within the required range as described previously. One difference is that the list of valid hydrogen/halogen bonds is computed on the fly for each configuration rather than storing a list based on the initial geometry. This corresponds to enforcing an update at each step in the original approach.

2.9. Consistency of the potential energy surface

One of the strengths of GFN-FF is that potential parameters are tailored based on the specific structure being studied. In particular, this comes from the initial bonding topology as defined by a pairwise cut-off. However, this can also create issues, since the answer obtained can sometimes depend on the starting structure prior to optimization. For example, depending on the initial lattice parameter used, some rock salt structured materials, MX, can either have bonds defined just between nearest-neighbors (i.e., metal-halide) or they can have additional bonds between next-nearest neighbors (e.g., metal-metal and/or halide-halide bonds). In an

extreme case, there could even be no bonds at all, which leads to a very different interaction model.

There are two aspects to the above problem that must be dealt with. Firstly, there is the issue of ensuring that calculations maintain the same parameters on restarting. Secondly, there is the question of defining the "correct" result for a given material when it depends on the starting point. Achieving consistent restarts is actually straight forward to address by saving the topology and parameters generated in the first run. Here we achieve this by capturing the initial structure and using this to regenerate the parameters on restart since this is a more concise way to capture the required information in the input file and the cost of determining the parameters is typically low. Finding a solution to the second issue is more complex. So far, we have yet to find a fully general solution. For dense ionic materials, it is possible to create a consistent initial geometry by re-scaling the closest neighbor distances to a specified fraction of the cut-off distance. However, for porous and network structures, this is more problematic. For now, the responsibility for the choice of a reasonable starting structure is left to the user, while options to control specific allowed bonds have been added (e.g., such as excluding metal-metal bonds).

2.10. Properties

The present implementation of (p)GFN-FF includes analytic second derivatives both with respect to Cartesian coordinates and/or strain. This allows the determination of the Hessian matrix for Newton-Raphson optimization with BFGS updating, as well as providing access to a range of material properties including the elastic constants, bulk and Young's moduli, piezoelectric constants, dielectric constants and acoustic velocities, to name a few of those available. The mass-weighted Cartesian second derivatives also provide the vibrational frequencies. In the molecular case, these can be corrected to remove rotational and translational mixing using Eckart purification. For solids, surfaces and polymers, it currently is only possible to compute the gamma point phonons, though other points in the Brillouin zone can be accessed

via the use of supercells. Extension to include direct phasing of all interactions to facilitate the calculation of phonon dispersion, etc., is planned for future work.

The pGFN-FF method, as described above, has been incorporated into a development version of the GULP code[25] so that the force field can be used in conjunction with all of the functionality available for solid-state calculations. Energy and first derivative evaluations can be performed in parallel using a shared memory MPI algorithm. Extension to include parallel second derivatives with distributed memory, in line with the rest of the code, is currently underway.

3. RESULTS AND DISCUSSION

Having described the implementation of the GFN-FF method for periodic systems, along with a number of suggested modifications to improve the suitability for such materials, we now examine how well this universal force field performs for a range of periodic systems. The aim is not to comprehensively cover all materials, but to provide illustrations of the strengths and weaknesses spanning some common systems of interest from (organic) molecular crystals, close-packed ionic solids and layered systems, through to framework materials, minerals and liquid water.

3.1. Molecular Crystals

In order to assess the performance of GFN-FF for molecular crystals, we compare lattice energies computed using GFN-FF with 'experimental' lattice energies derived from thermodynamic data measured experimentally as given in the X23 benchmark set.[26,27] This diverse set of well-determined molecular crystal structures consists of the original C21 set,[26] with the addition of hexamine and succinic acid. Unsurprisingly, experimental observations for these crystals were not at 0 K, so the 'experimental' lattice energies are back-corrected for the vibrational term and over time there have been revisions to the original energies. For this work, we use the recently revised X23b[28] reference energies (unless otherwise specified). The

accurate reference values facilitate examining the effects of modifications to the GFN-FF procedure described here as part of the pGFN-FF scheme – in this case the Wolf sum for topological charges and the use of damped three-body dispersion – along with how these modifications may interact with one-another.

To this end, each of the crystal structures in the X23 set were optimized starting from their experimental structure; i.e., X-ray diffraction structures from the CSD. The lattice energies were subsequently calculated relative to the gas-phase molecular structures optimized using the same settings, and subtracting these energies from the total crystal energy with consideration to Z, the number of formula units in the crystal.

Performance for molecular crystal lattice energies: The resulting lattice energies for the X23 set are shown in Figure 1. GFN-FF almost universally over-binds molecular crystals, evidenced by the mean signed error (MSE) and mean absolute error (MAE) being almost the same in magnitude. It is evident that introducing three-body dispersion damping significantly improved energetic performance overall, and that the introduction of the Wolf sum either further improved performance or at least did not introduce additional errors.

Figure 1. Deviations of the lattice energy from the reference values of the X23b set of molecular crystals.[28] The grey shaded region represents the mean energy from a variety of DFT methods,[29] with upper and lower bounds being plus or minus one standard deviation. Results are shown for four variants of GFN-FF (Orig.=original implementation; W=Wolf sum; dATM=damped ATM 3-body dispersion term).

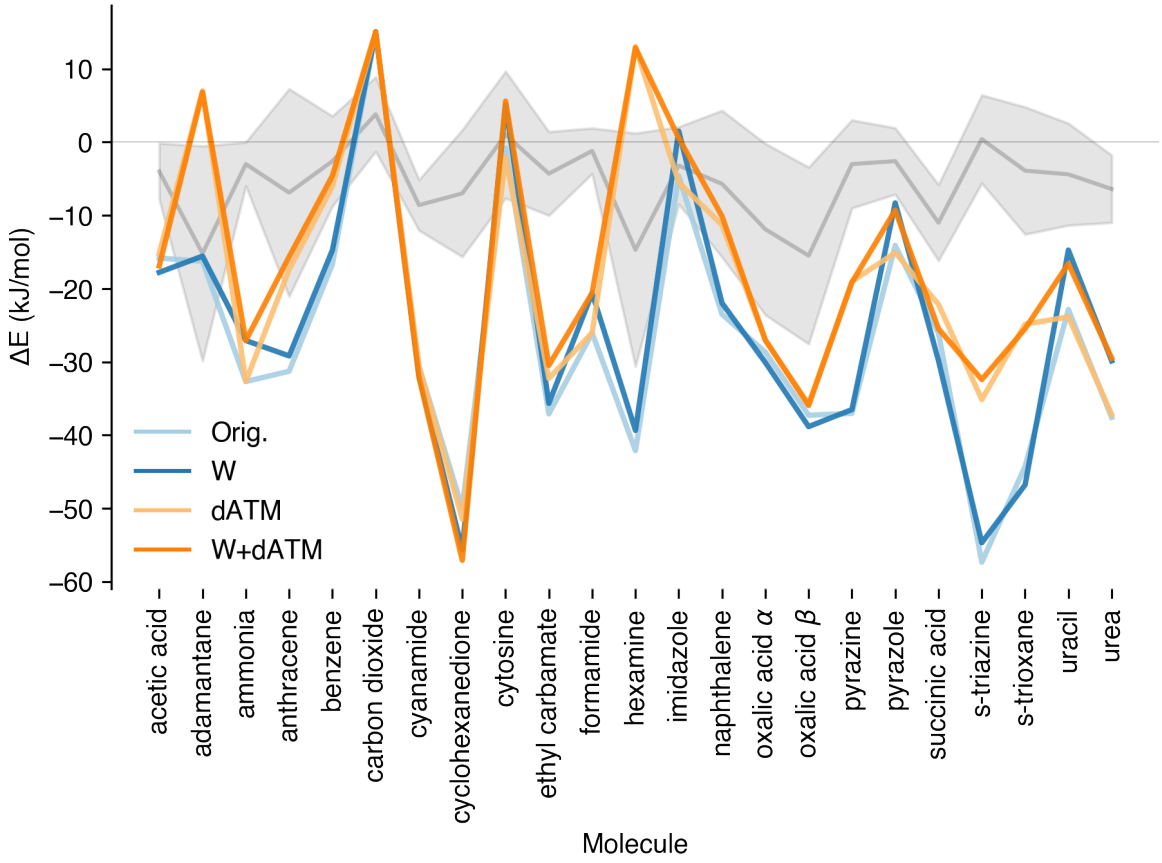

Performance overall (MSE/MAE -17.2/20.7 kJ/mol) is unsurprisingly worse than DFT methods, e.g., PBE-D3 (-1.8/4.1 kJ/mol)[30] or tailored rigid-molecule forcefields like FIT[31] (7.9/9.1 kJ/mol) and revised W99[32] (13.9/14.1 kJ/mol)[1]. However, when taking into consideration the generality of the approach, and the lack of molecule-specific parameters (FIT and W99 utilize multipole expansions for electrostatics derived from a molecular wavefunction), GFN-FF performs quite well, and offers a unique value proposition. Further, the original GFN-FF force field was never parameterized using crystalline systems, so were it to be re-parameterized incorporating crystalline systems then its performance should improve.

Performance for molecular crystal structures: Since the crystal structures were optimized starting from the experimental structure, it is worth identifying which structures remained correct, and which relaxed to alternative structures. The crystal geometries were not very sensitive to introduction of the Wolf sum or three-body dispersion damping (see Tables S2 and S3), and utilizing these settings yielded the best overall results. Therefore, the following discussion will focus solely on the results obtained with these settings.

The energetic over-binding of GFN-FF for molecular crystals is evident in the cell volume changes (see Figure S1). On average the unit cell volumes were approximately 18% smaller after optimization. While some of this contraction may be attributed to thermal expansion, the contraction is significantly larger than would be reasonably expected (for reference, DFT volumetric expansion results from Dolgonos *et al*.[28] have a maximum reported expansion of ~13% using PBE-D3 for s-triazine compared to the ~30% discrepancy seen here when using GFN-FF).

Putting aside the exaggerated volume contraction, the majority of the optimized crystal structures were correct to within appropriate tolerances. Indeed 12 of the structures, namely

[1] For PBE-D3, FIT and W99, MSE and MAE are taken from Ref 30, Table 1. These values were obtained from comparisons against older reference values for the X23 benchmark set, but the differences will be insignificant for the purposes here.

ammonia, adamantane, benzene, carbon dioxide, hexamine, imidazole, pyrazine, s-triazine, s-trioxane, succinic acid, urea and uracil were excellent matches to their reference crystal structures. Given the sensitivity of molecular crystal structures to subtle changes in the potential energy surface, it is not surprising that GFN-FF produces 'incorrect' minima in several cases, but the cyanamide was structure was particularly poor, as the molecular geometry was no longer linear – and the crystal packing unsurprisingly incorrect (see Figure S2).

3.2. Close-Packed Ionic Solids

With the GFN-FF force field being promoted as a universal force field applicable to all elements in the periodic table up to radon, we now assess its performance beyond molecular solids, focusing first on a series of close-packed ionic solids. Within this broad class of compounds are the alkali halides ($M^{I}X$) and alkaline-earth oxides ($M^{II}O$) which are known to crystallize largely in the rock salt (B1) crystal structure, with the exception of CsCl, CsBr and CsI that adopt the cesium chloride (B2) crystal structure.[33,34] (The reader is referred to Figure S3, Supporting Information, for a description of the conventional unit cells of the prototypical materials for these crystal structures).

In recent years, several research groups have gathered the experimental structures for these ionic solids and have examined the performance of density functional theory (DFT) methods in describing the relative stabilities of these two phases, in addition to their mechanical properties (such as the bulk modulus).[33,34,35] These studies emphasized the importance of including dispersion corrections to conventional DFT methods in order to capture the correct relative phase stabilities of these materials, given that these long-range interactions (even beyond nearest-neighbor[36]) become a driving force for the stability of the crystal structures as the size, or polarizability, of the ions within the solids increases.[33,34] In addition to this, the close proximity of ions within these periodic systems prompted the need to appropriately damp the

van der Waals dispersion interactions at short interatomic distances to avoid divergence in the dispersion terms.[33] As mentioned in earlier sections, the use of an undamped three-body dispersion term within the original GFN-FF implementation potentially leads to divergences in the computed van der Waals interaction terms for certain configurations of ionic solids (such as CsCl), which can ultimately cause the unit cell to "collapse" during geometry optimization.

While the aforementioned DFT studies were mainly focused on determining relative cohesive energies of simple ionic solids, we note that this may not always be possible to replicate (or even assess at all) with the GFN-FF force field. While this force field is considered to be dissociable (i.e., bonds between two atoms may be broken to yield separate non-interacting atoms), it does not allow for new bonds to be formed.[8] Thus, unlike other force fields (such as UFF or models parametrized specifically for halides[36,37]) which can be formulated in terms of purely pairwise repulsive and dispersive interactions with no additional (covalent) bonding terms, the GFN-FF force field is unable to describe processes that involve changes in bonding topology. As a result, if one considers the cations and anions within the ionic solid in either the rock salt or cesium chloride phases to be (covalently) bonded to each other at the onset of a GFN-FF calculation, then comparing energies between these phases will not be appropriate, as atoms are bonded to a different number of neighbors (6 and 8 for the rock salt and cesium chloride phases, respectively). Conversely, comparing any two phases where atoms share the same coordination numbers and bonding topologies may be possible, such as for the case of the two experimentally stable phases of ZnS, sphalerite and wurtzite, which have been previously studied with force field methods.[38]

It can be debated as to whether the ions in these nominally ionic solids should be considered to be covalently bonded or not to their neighbors, and whether energy terms for bonding, angle, torsion, etc. should be included in the total energy as the GFN-FF formulation intends. Here we examine the influence of controlling whether ions are covalently bonded or not, rather than

just allowing the criteria within GFN-FF to determine the topology based on the initial geometry. Performing pGFN-FF calculations while suppressing all covalent bonding terms between the ions in these metal halides and oxides largely led to structures being dynamically and/or mechanically unstable. Furthermore, in cases where stability was not an issue, the lattice parameters were severely overestimated. Only for a few intriguing cases (specifically RbBr, RbI, and for two of the three cesium halides in the B2 phase, CsCl and CsBr), did removing all covalent bonds lead to what seemingly were improved results in terms of lattice parameters compared to experimental values (see Table S4). These results suggest that suppressing covalent contributions in the GFN-FF formulation is generally inappropriate, even when they are counter-intuitive for ionic solids, or any system where atoms would be considered to be bound by ionic, rather than covalent, interactions. Future improvements to the non-bonded repulsion interaction could potentially alter this situation.

Given the above findings, we ensured that for all further calculations the reference configurations of each alkali halide or alkaline-earth oxide had ions and their immediate oppositely-charged nearest neighbors covalently bonded, while any bonds between two like metal or halide ions were explicitly suppressed. This resulted in each ion being bonded to 6 and 8 ions for the B1 and B2 phases, respectively. Each structure was then subjected to unconstrained geometry optimization in order to determine their lattice parameters and elastic/mechanical properties (represented here by the (static) adiabatic bulk moduli, though the full elastic tensor is available). The effect of utilizing various options and/or settings suggested to improve the robustness of the method – the use of the Wolf sum and/or a damped 3-body ATM dispersion term – as discussed in earlier sections was also examined. The overall performance of different variants in comparison to UFF is captured in Table 1, while full results are available in the SI (see Table S4).

Table 1. Statistics on deviations of conventional unit cell lattice parameter (Δa in Å), and adiabatic bulk moduli (ΔB_S in GPa), relative to experimental measurements for the alkali halide and alkaline-earth oxide materials studied herein as predicted by the periodic GFN-FF implementation (using various settings: Orig.=original implementation; W=Wolf sum; dATM=damped ATM 3-body dispersion term) and the UFF force field (using various settings: 0=atomic charges set to zero; QEq=atomic charges obtained from the charge equilibration method; see Table S4). MSE: Mean Signed Error, MAE: Mean Absolute Error, RMSE: Root-Mean-Square Error.

Method	Settings	Δa			ΔB_S		
		MSE	MAE	RMSE	MSE	MAE	RMSE
Alkali halides, $M^{I}X$ (N=20)							
GFN-FF	Orig.	-0.382	0.456	0.340	7.4	10.6	9.5
	W	-0.382	0.455	0.340	8.6	11.1	8.5
	dATM	-0.340	0.417	0.316	9.3	11.5	8.5
	W+dATM	-0.344	0.416	0.309	10.1	11.8	7.8
UFF	0	0.878	0.878	0.393	-22.5	22.5	13.7
	QEq	-0.632	0.632	0.159	73.6	73.6	62.5
Alkaline-earth Oxides, $M^{II}O$ (N=4)							
GFN-FF	Orig.	0.162	0.162	0.073	-52.8	52.8	31.3
	W	0.192	0.192	0.079	-52.3	52.3	28.5
	dATM	0.224	0.224	0.085	-49.3	49.3	30.0
	W+dATM	0.200	0.200	0.073	-50.8	50.8	26.9
UFF	0	1.637	1.637	0.272	-108.5	108.5	34.6
	QEq	0.385	0.385	0.258	-67.5	67.5	35.8
Total (N=24)							
GFN-FF	Orig.	-0.292	0.407	0.372	-2.6	17.6	27.2
	W	-0.286	0.411	0.379	-1.5	18.0	26.7
	dATM	-0.246	0.385	0.358	-0.5	17.8	26.2
	W+dATM	-0.253	0.380	0.349	0.0	18.3	26.2
UFF	0	1.004	1.004	0.470	-36.9	36.9	37.2
	QEq	-0.463	0.591	0.419	50.1	72.6	79.0

Of particular significance, damping the ATM 3-body dispersion term was found to help prevent the collapse of crystal structures due to (sometimes attractive) diverging ATM terms. Ionic solids with very polarizable atoms/ions, such as CsCl (see Figure S5) were found to benefit most from this methodological change, which meant geometry optimizations were less sensitive to the choice of initial geometry used for the calculation (e.g., experimental or benchmark geometries, or geometries obtained from computational databases like the Materials Project,[39] or even unit cells constructed from interatomic distances based on empirical ionic radii,[40] see Figure S3), provided of course that the initial bonding topology and coordination environment remained the same. That is, unless structures were compressed extensively, then no additional bonding, angle or torsion terms, or changes in coordination number/hybridization state, altered the bonding topology. Ultimately, choosing to utilize a damped ATM term in these calculations had little to no effect on the optimized lattice parameters, with the exception of expected ionic solids containing the larger and/or more polarizable ions, such as for the series of rubidium and cesium halides (see Figure S4A).

The Wolf sum was found to provide more intuitive results in terms of attributing the expected polarity for the ions within the ionic solids (i.e., cations having a positive charge and anions being negatively charged, instead of the opposite). While there did not seem to be any trend as to where counter-intuitive charges might occur when using the original GFN-FF formulation (see Figure S6), changes in computed lattice parameters remained minimal (LiF and BaO being two of the more notable exceptions), whereas computed bulk moduli were more significantly impacted. This is a consequence of the topological charges having a direct influence on the force constant for the bonds, rather than the equilibrium distance.

Absolute deviations between computed and experimental conventional unit cell parameters and adiabatic bulk moduli are presented in Figure 2. Given that utilizing the Wolf sum and a damped ATM term provided better stability and/or robustness to the (p)GFN-FF

implementation, we now focus only on these results for the remainder of the discussion (however, all other data points for the various settings can be found in Figure S4).

Figure 2. Deviations of computed values for the conventional lattice parameter, Δa, and adiabatic bulk moduli, ΔB_S, relative to experimental values, a_{expt} and $B_{\mathrm{S,expt}}$, for each of the alkali halide ($M^{I}X$ with X=F,Cl,Br,I) and alkaline-earth oxide ($M^{II}X$ with X=O) structures studied here. Only the results for the pGFN-FF method, which utilizes the Wolf sum and a damped 3-body ATM dispersion term, are shown. Figure S4 (Supporting Information) contains the remainder of the results for the other variants of GFN-FF examined.

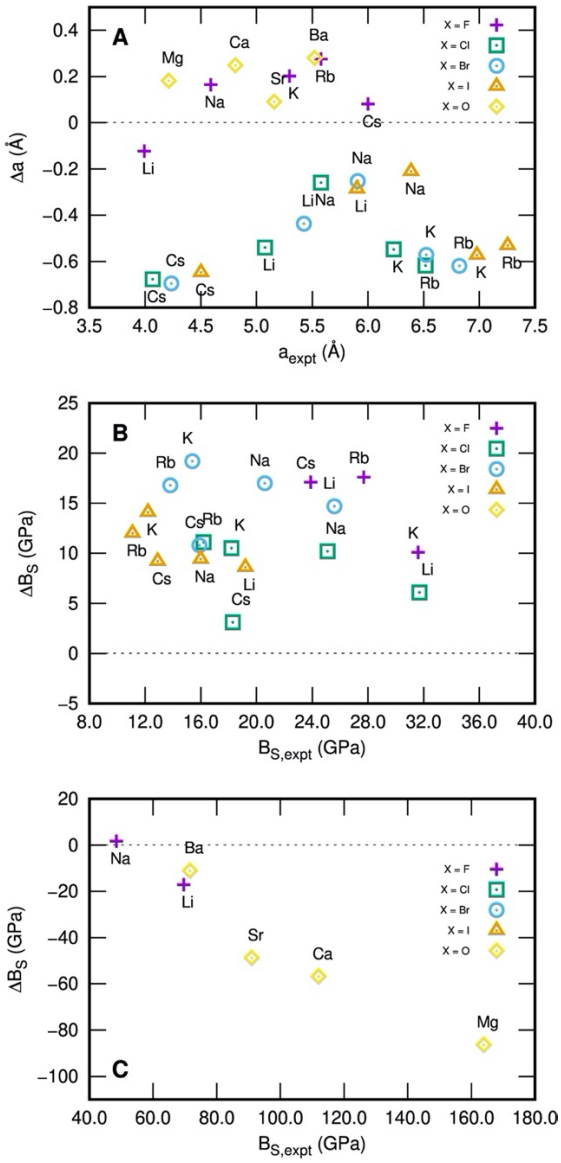

The computed unit cell lengths were generally found to be overestimated by ca. 5% on average for the $M^{I}F$ and $M^{II}O$ solids, whereas other halides had largely underestimated parameters by ca. 10-20% relative to the experimental values. In particular, the cesium halides in the B2 phase (X = Cl, Br, and I) represented the largest outliers *versus* experiment. For most of the other alkali halides (M = Li, Na, Rb, Cs), the magnitude of the underestimation for the unit cell parameters largely follows the order $M^{I}Cl > M^{I}Br > M^{I}I$, although the reverse is true for the potassium halides. Whether in these cases this is due to a suboptimal description of the covalent bonding and electrostatics terms as a function of primarily the alkali metal (ions within alkali halides having similar partial charges regardless of the element), of dispersion interactions (being overestimated for smaller/less polarizable ions interacting with larger/polarizable ions, and *vice versa*), or from an imbalanced description between these terms (given the opposite trend to varying the halogen atoms within the potassium halides, as opposed to other alkali halides), remains to be explored.

Overall, the deviations in predicted unit cell parameters to experimental values are not unexpected for a force field, let alone one that is meant to be universal (see Table 1). The mean signed and absolute errors are within reasonably acceptable values, and provide slightly better results than UFF (regardless of whether one fixes charges to zero or uses charges obtained through charge equilibration methods), with pGFN-FF slightly outperforming both in terms of mean absolute errors and spread of the data (RMSD values). Unlike UFF, pGFN-FF does however provide situations where the unit cell parameters are underestimated, while some systems are overestimated ($M^{I}F$ and $M^{II}O$). Compared to static lattice constant values computed by high-level dispersion-corrected DFT which display MSE's and MAE's ranging from ca. 0.04–0.4 Å (although these are obtained from comparing experimental values back-corrected for zero-point vibrational effects – having but a minor effect on the absolute value for the lattice constant of alkali halides, ca. < 0.005 Å), pGFN-FF performs on par with some of the worst-

performing of these methods. This is a reasonable result, given the significantly lower cost of force field calculations compared to these other methods.

In terms of predicting the (static) adiabatic bulk moduli, pGFN-FF also performs very well (with a notable exception discussed below), yielding a mean absolute error just shy of 18.5 GPa for the complete set of alkali halides and alkaline-earth oxides with respect to experimental values. While it has been pointed out that comparison of these computed static bulk moduli with experimentally-measured values is not appropriate and can lead to erroneous conclusions on the suitability of a method at correctly computing these properties, given that the bulk modulus is substantially affected by changes in temperature,[35] we stress here that the computed MAE values for pGFN-FF are very much in agreement with static bulk moduli computed by appropriate dispersion-corrected DFT methods (which in these cases had MAE's ranging between ca. 5–15 GPa). In general, the predicted bulk moduli for the ionic solids all seemed to show clustering as a function of the anion more so than the cation; the largest range in errors occurring with decreasing order $M^{II}O >> M^{I}F > M^{I}Cl \sim M^{I}Br > M^{I}I$, with the bulk moduli for the $M^{II}O$ being more greatly underestimated relative to experiment (or even DFT computations[35]), and the bulk moduli of the alkali halides generally being overestimated in decreasing order $M^{I}Br > M^{I}I > M^{I}Cl$ with $M^{I}F$ (see Figure 2B and C). Notably, pGFN-FF fails to predict reliable bulk moduli for the alkaline-earth oxides. These results echo similar substantial underestimations in bulk moduli predicted for the sphalerite and wurtzite phases of ZnS (Table S5). It has long been noted that the computed hardness of ionic materials tends to be strongly correlated with the choice of charges used. For ions with a formal charge greater in absolute magnitude than 1 most force fields overestimate bulk moduli unless partial charges are used. However, the charges generated for $M^{II}O$ in pGFN-FF are arguably too low, being less than +0.4 for the metals (Figure S6), such that these are not adequately compensated for by the force constants of the metal-oxygen covalent bonds. Despite this, pGFN-FF succeeds in

terms of outperforming its competitor UFF for bulk moduli of ionic solids (barring neglect of zero-point vibrational and thermal effects).

3.3. 2D Layered Materials

Layered materials have attracted much interest over the past decade or so due to their promising applications as lubricants, ion transport materials, spintronic and optoelectronic devices, and more.[41] Although graphene is the most well-known and studied of these materials so far, a vast array of other layered structures, such as hexagonal boron nitride, and various transition-metal dichalcogenides, and oxides, have since been examined due to their varied optoelectronic properties.[42,43] In addition to these materials, the many recent ventures into the development of 2D layered (either all-inorganic[44,45] or hybrid organic-inorganic[46,47,48]) perovskite heterostructures – materials which promise to provide improved solar cell/photovoltaic devices[49,50] – also speaks to an increased interest in such materials. However, designing materials or devices that consist either completely (or partially) of a 2D layered structure and which have specific properties can prove to be a challenging task from both an experimental and/or computational point of view, given the vast number of factors which can influence the physical, chemical, and optoelectronic properties.[42,44,45,47,49,50]

The utility of a universal force field like GFN-FF, being orders of magnitude faster than conventional *ab initio* methods, for studying complex material architectures is evident, especially if one is interested in screening a large number of potential structures or performing high-throughput analyses of materials in order to identify candidates with desirable physical and/or mechanical properties. In this section, we aim to highlight the various considerations which should be kept in mind when utilizing (p)GFN-FF in order to study 2D layered structures.

Exfoliation (or binding) energy curves: It has been suggested that "establishing high thermal and chemical stability of a 3D material is essential before contemplating its 2D counterpart".[42]

Benchmark sets of (bulk) layered materials have indeed been assembled in order to assess a computational method's ability at reproducing not only accurate lattice parameters for these crystal structures, but also interlayer binding energies (which are approximately equal to exfoliation energies, and in turn indicative of whether formation of atomically thin layers is feasible).[51,52]

For the purposes of examining the capabilities of pGFN-FF at reproducing structural parameters and binding energies for representative semiconducting materials, we chose the set assembled by Bjorkman and co-workers,[51,52] although we note that more restrained[53] and ever expanding[43] sets/databases exist. This particular set consists of hexagonal crystal structures of graphene and boron nitride (h-BN), various trigonal (1T-) or hexagonal (2H-) crystal structures of transition-metal dichalcogenides (TMDCs, with an MX_2 structure; M being a transition metal, and X being either S, Se or Te), along with the tetragonal lead oxide (2Q-PbO) structure (see Figure S7 for a more detailed description of these crystal structures). The most accurate reference data available for these layered materials (at least in terms of binding energies) was provided by RPA calculations, given that there is currently a lack of data with more accurate computational methods (such as Quantum Monte Carlo methods) and that there are often large uncertainties in experimentally determined measurements of exfoliation energies.[52]

In order to determine the binding energies of the structures in this set, we first performed geometry relaxations for each structure (allowing for both intra- and inter-layer degrees of freedom to be relaxed). Binding energy curves (such as those illustrated in Figure 3) were then generated by varying the inter-layer separation in small increments, from slightly below the equilibrium value and up to the limit of large inter-layer separations (where slabs have negligible interaction), while performing energy evaluations at each of these incremental values. It is important here to note that allowing the force field parameters to be determined based on the actual structure for every point along these binding energy curves can lead to

discontinuities in the potential energy surface, especially at small inter-layer separations (see Figure 3). These discontinuities arise because of either new coordination and/or bonding environments occurring for atoms that interact with neighboring layers, where no covalent interactions should occur. Therefore, if care is not taken to either fix the GFN-FF parameters based on a suitable reference geometry (e.g., at, or close to, the experimental geometry), or by explicitly ensuring that no bonds can form between atoms that are part of two different layers, then an incorrect or discontinuous binding energy curve may be obtained. Care should also be taken so as to not exclude bonds between atoms within a given slab of the material (e.g., disabling all C-C bonds in graphene leading to a non-bonded system, as opposed to only disabling bonds between C atoms of different layers).

Figure 3. Binding energy curves for graphene (panels A and B) and 1T-HfS_2 (panels C and D). Δz represents the deviation of the equilibrium lattice parameter along the c-axis, whereas the binding energy, ΔE, is relative to two infinitely separated slabs of the layered material. Various binding-energy curves are depicted to illustrate the effect of (1) allowing the force field parameters to be determined by pGFN-FF for each point of the scan ("on-the-fly"), or keeping them fixed based on (2) expanded or (3) compressed reference geometries (using the specified Δz value), or ensuring that bonds between specified atoms are removed (either all (X-X) bonds or only bonds between atoms that are part of two different layers (e.g., X1-X2)) are shown. Panels B and D depict an expanded view of panels A and C, respectively, in the region close to $\Delta z = 0$.

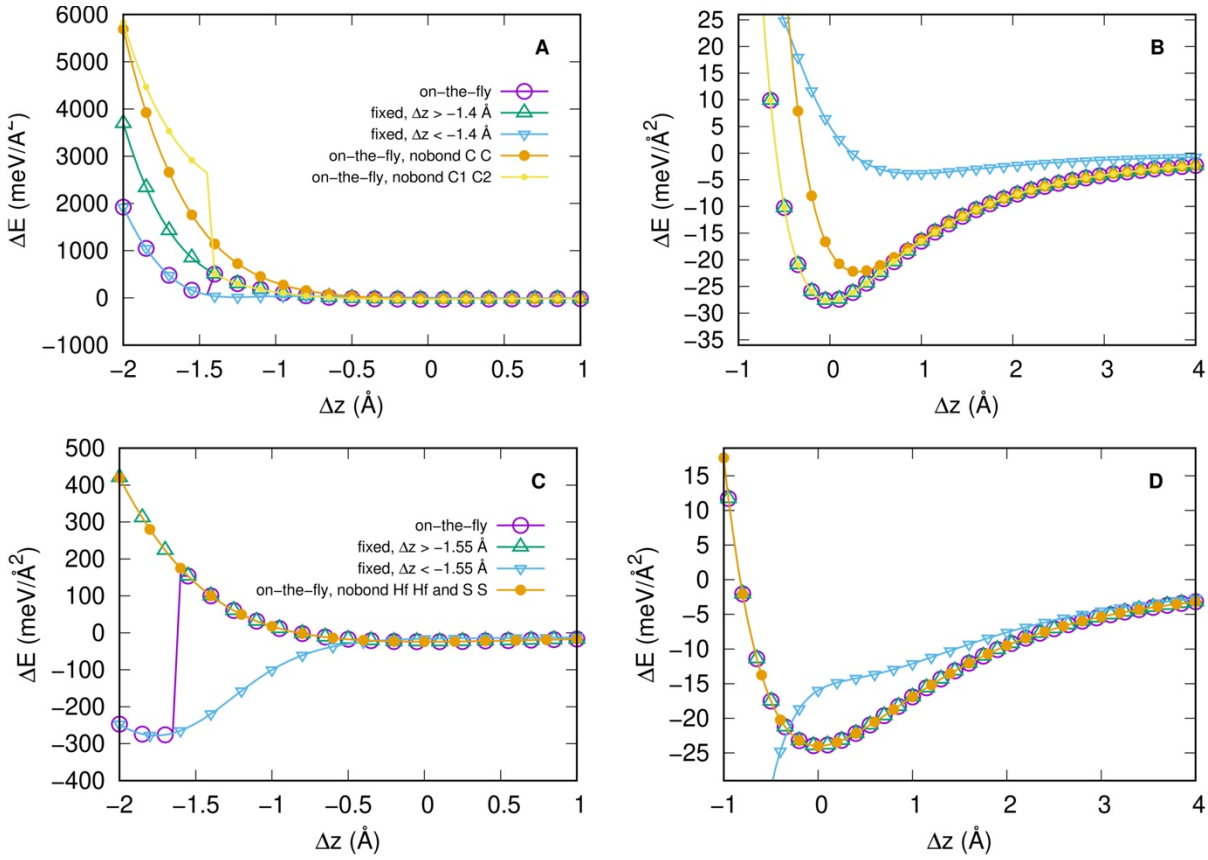

Results for the deviations of unit cell parameters and binding energies for the structures examined here are shown in Figure 4. Focus is again placed on results obtained with the pGFN-FF method, which makes use of the Wolf sum and a damped ATM term. Results for the original GFN-FF method, along with either and/or both of the other settings, can be found in Tables S7 and S8. These results show that the Wolf sum aids in reversing the charge polarity in cases where these were counter-intuitive (i.e., for h-BN and PbO, where the less electronegative atoms were initially found to have negative partial charges, and *vice versa*) and in reducing the magnitude of these initial topological charges ($HfTe_2$ and $ZrTe_2$ being notable cases where the assigned partial charges were substantially larger in the reference configuration compared to all other layered materials). The use of a damping of the ATM term proved important to avoid structural collapse for PtS_2, which faced similar issues to the CsCl structure noted in the previous section. However, utilizing only the damped ATM term (without the Wolf sum used to determine topological charges), led to an increased interlayer spacing within the structures just highlighted (PbO, PtS_2, $HfSe_2$, and $ZrTe_2$). The nature of the ATM term tending to be a largely repulsive contribution to the dispersion energy has been noted before,[54] and so these results are not unexpected given that the ATM term within the original GFN-FF implementation (as is the case in this work) is dependent on the partial charges assigned to each atom within the system. Therefore, in many cases, this contribution, when repulsive, can be exaggerated if the assigned partial charges are equally large in magnitude.

Figure 4. Deviations of computed values for the conventional lattice parameters, Δa and Δc, and binding energies, ΔE, relative to experimental and RPA values, a_{expt}, c_{expt}, and $\mathrm{E_{RPA}}$, respectively, for each of the layered materials that are part of Björkman's set.[51] Only the results for the pGFN-FF method, which utilizes the Wolf sum and a damped 3-body ATM dispersion term, are shown; results for other variants of GFN-FF, as well as the UFF force field, are tabulated in the Supporting Information (see Tables S7 and S8). Panel B omits the results for MoS_2, $MoTe_2$, and WSe_2 for clarity (Δc = 9.3, -0.6, and 9.2 Å, and c_{RPA} = 12.302, 13.973, and 12.960 Å, respectively). Panel C omits the result for $PdTe_2$ for clarity ($\mathrm{E_{RPA}}$ = 40.1 meV/Å^2 and ΔE = -12.4 meV/Å^2).

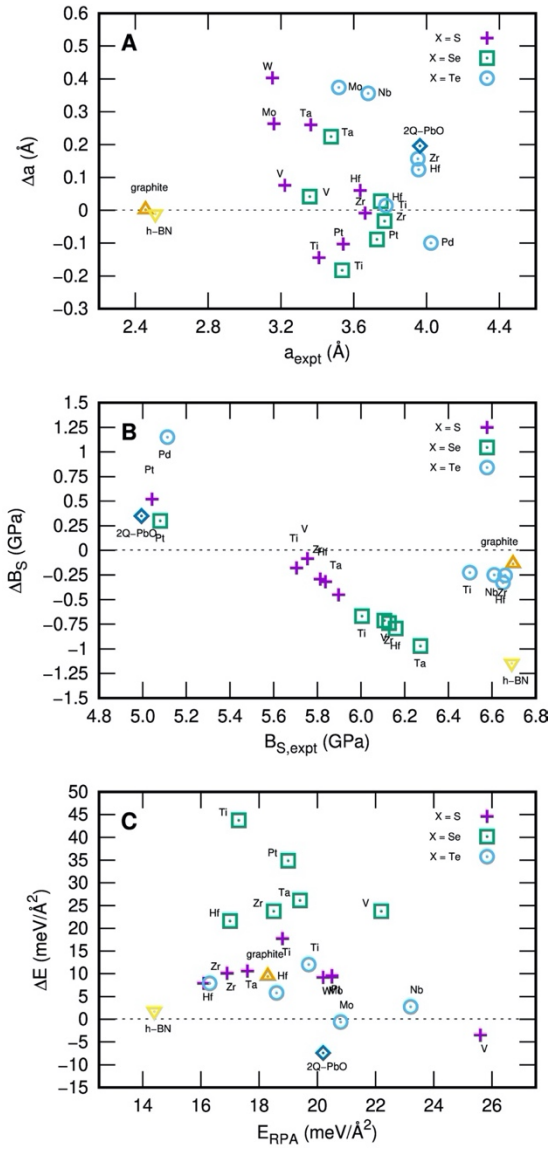

There is a clear tendency of (p)GFN-FF to overestimate the binding energies for these structures (see Figure 4C), which is largely due to the (interlayer) unit cell parameters being significantly underestimated relative to the reference values (Figure 4B). This points to interactions between adjacent layers that are too strong, potentially as a consequence of the dispersion terms (a modified/simplified D4 scheme,[8] with a damped or undamped ATM contribution) most likely having too large homoatomic dispersion coefficients for the chalcogen atoms involved.[54] The results obtained with (p)GFN-FF for these materials are therefore expected, given the force field will undoubtedly inherit any characteristics of the models utilized to computed the different energy contributions (let alone those that come from fitting the parameters to reproduce specific theoretical reference data (B97-3c and/or PBEh-3c geometries, frequencies, and other theoretical data[8]). These observations are reflected in terms of overall performance of (p)GFN-FF at describing geometries and binding energies (see Table 2). While more or less competitive with UFF, the computed MAE's for (p)GFN-FF are in line with errors computed by DFT methods, at least energetically, that make use of dispersion corrections of the same class.[52,53,54] For instance, the MAE's for binding energies reported for PBE-D3(BJ) optimized geometries for all 26 systems studied here were found to be 14.16 meV/Å^2,[54] as compared to 13.5 meV/Å^2 from the present model.

Table 2. Statistics on deviations of conventional unit cell lattice parameters (Δa and Δc in Å), and binding energies (E in meV/Å^2), relative to experimental measurements for the 2D layered materials part of Björkman's set[52] as predicted by the pGFN-FF implementation (using various settings: Orig.=original implementation; W=Wolf sum; dATM=damped ATM 3-body dispersion term) and the UFF force field (using various settings: 0=atomic charges set to zero; QEq=atomic charges obtained from the charge equilibration method; see Table S9). MSE: Mean Signed Error, MAE: Mean Absolute Error, RMSE: Root-Mean-Square Error.

Method	Settings	N	Δa			Δc			E		
			MSE	MAE	RMSE	MSE	MAE	RMSE	MSE	MAE	RMSE
Sulfides, MS_2 (N=8)											
GFN-FF	Orig.	7 [a]	0.119	0.170	0.178	-0.453	0.453	0.296			
	W	8	0.094	0.168	0.186	-0.295	0.437	0.411			
	dATM	8	0.150	0.189	0.174	-0.281	0.545	0.578			
	W+dATM	8	0.101	0.165	0.180	-0.303	0.433	0.399	8.9	9.7	5.4
UFF	0 [b]	7 [b]	0.096	0.195	0.199	0.166	0.436	0.565	-8.4 [e]	8.4 [e]	2.4 [e]
	QEq	8	-0.016	0.162	0.187	-0.469	0.586	0.564	-7.4	7.4	2.0
Selenides, MSe_2 (N=9)											
GFN-FF	Orig.	6 [c]	-0.104	0.123	0.146	-0.545	0.720	0.484			
	W	6 [c]	-0.021	0.112	0.143	-0.578	0.717	0.456			
	dATM	6 [c]	-0.024	0.084	0.100	-0.640	0.712	0.388			
	W+dATM	6 [c]	-0.002	0.100	0.126	-0.598	0.698	0.413	28.9	28.9	7.8
UFF	0	9	0.164	0.193	0.142	0.390	0.390	0.324	-11.3	11.3	1.3
	QEq	9	0.116	0.155	0.139	0.412	0.412	0.321	-10.8	10.8	1.3
Tellurides, MTe_2 (N=6)											
GFN-FF	Orig.	6	0.236	0.336	0.298	0.041	0.410	0.572			
	W	6	0.116	0.191	0.196	0.079	0.402	0.550			
	dATM	6	0.173	0.209	0.175	0.191	0.390	0.471			
	W+dATM	6	0.154	0.188	0.170	0.044	0.397	0.521	2.6	6.9	7.8
UFF	0	6	0.154	0.219	0.175	0.532	0.532	0.522	-14.7	14.7	7.3
	QEq	6	0.115	0.184	0.166	0.556	0.556	0.515	-14.4	14.4	7.4
Total (N=26, incl. graphite, BN, and PbO)											
GFN-FF	Orig.	22 [a,c]	0.078	0.185	0.239	-0.280	0.572	0.626			
	W	23	0.063	0.145	0.176	-0.269	0.520	0.553			
	dATM	23	0.099	0.151	0.169	-0.220	0.584	0.654			
	W+dATM	23	0.083	0.141	0.166	-0.291	0.507	0.525	11.5	13.5	12.8
UFF	0	24 [b,d]	0.095	0.198	0.203	0.163	0.445	0.577	-9.5 [e]	11.4 [e]	7.8 [e]
	QEq	26	0.048	0.173	0.203	0.146	0.471	0.613	-7.7	11.0	9.1

[a] In this case (1T-PS_2), the geometry optimization leads to the unit cell imploding, due to the dispersion term tending to -∞ (largely a consequence of the undamped 3-body ATM term and the optimizer over-stepping during the line-search, as was the case for the B2 phase of CsCl described in the main text).
[b-e] Structures are predicted to be dynamically unstable; in addition, performing geometry optimizations while constraining the cell to be orthorhombic results in the AB-stacked structure shearing and yielding the AA-stacked structure instead. Structures affected: [b] 2H-WS_2; [c] $MoSe_2$, $NbSe_2$, and WSe_2; [d] h-BN; [e] 2H-WS_2; [f] 1T-TaS_2.

It should be noted that for some of the 2H-MSe_2 structures (with M = Mo, Nb, and W), imaginary modes were obtained during the unconstrained geometry relaxations and could not be removed without either the cell shearing (or if the cell was restrained to be orthorhombic, adjacent layers shearing) in order to yield the AA-stacked, instead of the AB-stacked, configuration. Regardless of the specific variant of GFN-FF used for these materials, the AB-stacked configuration was never a stable configuration.

Lattice mismatch, internal strain, and thermal expansion coefficient measurements: There is a myriad of potential applications where the (p)GFN-FF method could be extremely useful given its expediency in providing results for crystal structure geometries and mechanical properties, in contrast to the often-prohibitive costs which limit the scope and applicability of *ab initio* methods. In particular, much attention is currently being placed on high-throughput screening of complex 2D-layered perovskite architectures in an effort to improve upon the instability issues that impede commercialization of these materials. Aspects that could be improved include minimizing instabilities due to moisture, air or heat, while gaining an understanding in how internal strain (due lattice and/or thermal expansion mismatch) imparted by stacking various perovskite layers with other substrates, such as protective coatings,[55] during the fabrication of photovoltaic devices can lead to alterations in their stability (unwanted "black-to-yellow" phase transitions) and perhaps even their optoelectronic properties[56,57,58,59] For even the simplest of theoretical models for predicting strain due to lattice mismatch,[55] let alone some of the more sophisticated ones,[60] this can prove to be difficult if one is constrained to using high-level calculations to obtain reliable results.

While a detailed examination of whether or not pGFN-FF can provide accurate results for this application is beyond the scope of this paper, we can highlight several complications that may occur when studying more complex ionic solids (in contrast to the earlier systems studied above) such as for perovskites. Here, we take a commonly studied perovskite material, $CsPbI_3$

in its cubic phase (with space group $Pm\bar{3}m$) to illustrate a few points of interest, including a comparison with the results of a recent study using the AMOEBA force field.[61]

The ideal cubic perovskite structure for ABX_3 consists of a 3D network of corner-sharing BX_6 octahedra, where B is a cation (Pb, Sn, etc.) and X is an anion (O, F, Cl, Br, I, etc.), while the larger cation A (Cs, Rb, organic cations, etc.) is found at the center of cubic space defined by the octahedra with 12-fold coordination to the anions, X. In terms of performing pGFN-FF calculations, it has been made evident from previous sections that the reference bonding topology can potentially affect the outcome of geometry optimizations if care is not taken. The situation is no different in this case, although a greater degree complexity can arise depending on how one interprets the bonding between A, B, and X ions within the perovskite structure, and which initial reference structure is utilized as input for the calculation.

Figure 5 shows two different situations: either one allows bonds to exist between both B and X in addition to A and X ions (see Figure 5A), or only between B and X (see Figure 5B). In the first situation, this would mean that 18 covalent bonds (12 Cs-I and 6 Pb-I bonds) would be present in the initial bonding topology, whereas the second would lead to just 6 B-X (Pb-I) bonds. The latter is arguably the most intuitive description of the system, especially when extrapolating from the case of simple cations through to molecular cations on the A site. In either case, it is clear that depending on the choice of initial lattice parameters, geometry optimizations will lead to different potential energy surfaces being explored because of different bonding topologies, coordination environments and hybridization states being assigned to the ions within the crystal structure, which are kept fixed throughout the calculation. These overall changes in topology are reflected by the discontinuities present along the thick black curves in Figure 5, which have been constructed by performing single point energy calculations while varying the lattice parameter, thereby potentially allowing for a change in bonding topology to occur between different points.

Figure 5. Potential-energy curves for the $CsPbI_3$ cubic perovskite structure where the initial bonding topology (A) may or (B) may not include A-X bonds. The thick black line represents the total energy curve computed by pGFN-FF as the unit cell parameter, a, is varied, where the initial bonding topology is determined at each point along the surface. The total number of bonds (sum of A-X and B-X bonds; thick green curve) and number of separate fragments (thick blue line) are indicated by n along the right-hand y-axis. For each point where there are discontinuities (these are discussed in the main text), potential energy curves (thin-colored lines) are equally plotted by keeping the bonding topology fixed to the geometry of the closest point preceding the discontinuity. Inset structures show (A) $CsPbI_3$ with 12 Cs-I and 6 Pb-I bonds, and (B) $CsPbI_3$ with 6 Pb-I bonds. Atoms are colored as follows, Cs: green, Pb: gray, I: purple. The experimental cell parameter, a = 6.297 Å at 645 K (taken from Ref. 61) is shown by the black dashed line.

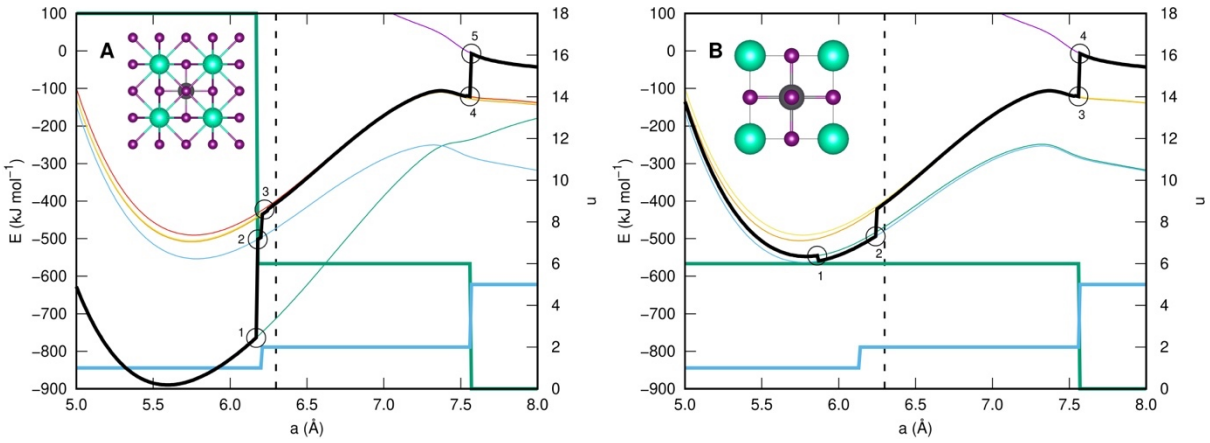

Once a starting point is chosen during a geometry optimization run (i.e., choosing an initial value for the lattice parameter), GFN-FF determines the bonding topology (which fixes the bond, bend and torsional terms, atom type and hybridization, amongst other things, based on interatomic distances and coordination environments), and in turn fixes the potential energy surface that will be explored. The set of distinct potential energy surfaces are represented by the thin-colored lines in Figure 5. For instance, if one performs a calculation with an initial cell parameter $a < 6.17$ Å, the optimization will proceed along the surface defined by the thin green potential energy curve, yielding an optimized unit cell with $a = 5.593$ Å. However, $a > 6.17$ Å causes the initial bonding topology to change. At the first point of discontinuity (point 1), the total number of bonds decreases from 18 to 6; i.e., only B and X ions are now bonded (similar to the scenario depicted in Figure 5B). However, if one starts with a unit cell parameter 6.17 Å $< a <$ 6.21 Å (point 2), GFN-FF now partitions the system into two separate fragments, which further changes the potential energy surface to be followed. In this case, GFN-FF ends up predicting a somewhat larger lattice constant, 5.748 Å, for the minimum energy geometry. The partitioning of the system into separate fragments within the original GFN-FF method is based on the neighbor list, which is distinct from the bonding neighbor list, and may imply (as just shown here), that changes in number of fragments may not occur simultaneously with the change in number of bonds. In order to address this issue (and to avoid additional discontinuities), an option has been added for pGFN-FF where it is the bonding topology, and not the neighbor list that controls how GFN-FF partitions the system into separate fragments. The result of using this option reduces the number of discontinuities and merges the point at which the system is split into an octahedral Pb complex coordinated to 6 I ions and a lone Cs cation (only one transition from point 1 to point 2 in Figure S8, as opposed to points 1, to 2, to 3 in Figure 5A). The other remaining discontinuities (i.e., at larger distances with a equal to ca. 6.21 Å and 7.56 Å, points 3 and 4 in Figure 5A), result from fluctuations in hybridization

states of the Pb ion; equilibrium angles that are inconsistent with the cubic perovskite structure may appear due to Pb being assigned an sp^3 hybridization state instead of the octahedral (sp^3d) hybridization state. This ultimately shifts the potential energy surface higher in energy, although the location of the minimum remains largely unaffected. Finally, if an extremely expanded geometry is utilized as the starting point, then no bonds are assigned between either Cs or Pb with I, and this results in exploring a purely repulsive potential-energy curve (point 5). Similar observations can be made in Figure 5B, where all Cs-I bonds have been suppressed. In this instance, all discontinuities point to changes in the hybridization state of the ions within $CsPbI_3$.

The importance of choosing an appropriate reference configuration for a GFN-FF calculation should be clear from the above discussion. In most cases, however, the observed minimum appears to be consistently captured (ca. 5.75 Å, aside from when the system consists of 12 Cs-I and 6 Pb-I bonds), despite the total energy of the system being highly variable depending on the force field description. For other properties of interest (e.g., mechanical properties) that depend on the curvature of the potential surface, the result does not appear to be greatly affected by the choice of input geometry (provided the number of bonds remains the same), which suggests that (p)GFN-FF could be usefully applied to screening of properties for such materials.

3.4. Metal-Organic Frameworks

Another significant family of materials where pGFN-FF can be applied is the simulation of the structural and mechanical properties of Metal Organic Frameworks (MOFs). Indeed, the original paper describing the GFN-FF force field highlighted the application to several such structures, though formulated as large clusters rather than periodic solids. The Cambridge Structural Database (CSD) contains more than 10,000 MOF structures, which display an incredible variety of metal centers and organic linkers, and a generic force field that can be

readily used to simulate any element in most of the periodic table will provide a unique opportunity to quickly screen hundreds of structures, which can then be further optimized and characterized with a higher level of theory.

Although a comprehensive benchmark of the structural properties of MOFs predicted by GFN-FF is beyond the scope of the present work, it is worth comparing its performance at least against another recently developed universal force field that was parameterized specifically for application to MOFs (UFF4MOF).[4] In Table 3, we report the lattice parameters, density, bulk modulus and shear modulus for a selection of the MOFs that were also previously optimized with UFF4MOF; we excluded $Ni_2(bdc)_2(dabco)$ and MOF-235(Fe) because the experimental structures that we found were disordered and the current implementation of GFN-FF does not support partially occupied sites via a mean-field description. A depiction of the unit cells for each MOF studied here can be found in the Supporting Information, Figure S9.

Table 3. Lattice parameters (a, b, and c in Å), density (ρ in g/cm^3), and elastic properties (bulk and shear moduli, B and G, respectively, in GPa) of selected MOFs as predicted by pGFN-FF (with Wolf sum and damped 3-body ATM dispersion term). Percentage errors are quoted for the pGFN-FF results relative to experiment. The experimental and UFF4MOF lattice parameters were taken from Ref. 62.

MOF	Experimental space group		Lattice parameters			Error %	Properties		
			Expt.	UFF4MOF	pGFN-FF		ρ	B	G
Cubic									
MOF-5	$Fm\bar{3}m$	a	25.8849	26.08	25.952	0.26	0.5852	8.5	0.9
IRMOF-8 [a]	$Fm\bar{3}m$	a	30.0915	30.34	30.276	0.61	0.4404	5.0	0.6
IRMOF-10 [a]	$Fm\bar{3}m$	a	34.281	34.55	34.620	0.99	0.3216	5.2	0.4
IRMOF-14	$Fm\bar{3}m$	a	34.381	34.52	34.414	0.10	0.3723	5.8	0.5
IRMOF-16 [a]	$Pm\bar{3}m$	a	42.9806	43.64	43.129	0.35	0.2031	3.6	0.3
HKUST-1(Cu)	$Fm\bar{3}m$	a	26.343	26.94	26.036	-1.17	0.9829	13.4	1.9
HKUST-1(Zn)	$Fm\bar{3}m$	a	26.520	27.49	26.079	-1.66	0.9863	12.4	2.4
HKUST-1(Ni)	$Fm\bar{3}m$	a	26.594	26.48	26.098	-1.87	0.9541	14.2	1.9
MFU-4(Co)	$Fd\bar{3}m$	a	21.731	20.98	21.001	-3.36	1.2976	21.6	6.5
MFU-4(Zn)	$Pm\bar{3}m$	a	21.6265	21.62	21.338	-1.33	1.2814	13.9	4.3
MFU-4l(Co_4Zn)	$Fd\bar{3}m$	a	30.995	31.18	30.749	-0.79	0.5645	10.4	2.3
Hexagonal									
MOF-177	P31c	a	37.072	37.65	37.310	0.64	0.4204	7.2	0.6
		b	30.033	30.51	30.100	0.22			
Orthorhombic									
MIL-53(Cr) [a]	Imma	a	6.812	6.60	6.537	-4.04	1.1171	5.9	5.0
		b	16.733	16.48	15.513	-7.29			
		c	13.038	12.66	13.610	4.39			
MIL-53(Al) [a]	Imma	a	6.608	6.51	6.532	-0.85	0.9804	20.2	8.2
		b	16.675	16.25	15.392	-7.69			
		c	12.813	12.49	13.913	8.59			
MIL-53(Fe) [a]	Imma	a	15.9624	15.62	15.455	-3.18	1.0895	15.3	5.3
		b	14.3920	13.98	13.946	-3.10			
		c	6.9351	6.61	6.675	-3.75			
Tetragonal									
DMOF-1(Zn) [a]	P4/mmm	a	10.929	11.31	10.792	-1.25	0.8967	12.0	4.0
		b	9.608	9.20	9.082	-5.47			
DMOF-1(Cu) [a]	P4/mmm	a	–	11.08	10.806	–	0.8868	13.8	3.3
		b	–	9.06	9.101	–			

[a] Structures were relaxed by constraining the cell to remain cubic, orthorhombic or tetragonal as appropriate.

The starting coordinates for all structures were taken from the CSD apart from IRMOF-8, IRMOF-10 and the DMOF-1 MOFs, which were taken from the CoRE MOF database.[62] All the structures were initially relaxed while preserving the experimental space group, apart from the structures taken from the CoRE MOF database (v1.1.3), which were already in P1

symmetry, where we constrained the cell to remain cubic (IRMOF-10 and IRMOF-16) or tetragonal (DMOF-1) as appropriate to the initial structure. The phonon frequencies were computed for all the relaxed structures, and IRMOF-10 and the MIL-53 showed imaginary modes that were removed by breaking the symmetry and relaxing the structures with orthorhombic or cubic constraints on the cell. In all cases the imaginary frequencies were related to small rotations of the phenyl rings of the organic linkers, which are averaged to a higher symmetry configuration in the crystallographic data.

Overall, the two force fields, UFF4MOF and pGFN-FF, perform similarly, and they appear to be generally consistent in under-/over-estimating the lattice parameters, which might be an indication that simple force fields may not be able to capture the complexity of the atomic interactions in MOFs. pGFN-FF is slightly better at reproducing the experimental lattice parameters of the IRMOF structures and slightly worse for the MIL-53 structures. Although a systematic comparison of the elastic properties of MOFs is beyond the scope of the present work, the bulk and shear moduli reported in Table 3 are in line with those of MOFs with similar densities that are listed on MOF-explorer database[63] hosted by the University of Cambridge.

3.5. Minerals

Minerals have been widely studied using force field methods over the last four decades due to their relevance to geology and geochemistry, as well as applications such as minerals processing. Obviously, there are a vast number of different minerals that exist and so a comprehensive study is not possible here. Instead, we choose to focus on two examples in detail to illustrate the performance of the current force field model for systems that can be classed as a 3D continuous network and a 2D layered structure with hydrogen bonding, while a general overview of the performance for minerals containing molecular anions will be given.

Arguably one of the most studied materials is α-quartz, as it is the most stable polymorph of SiO_2 at ambient conditions and high density end-member for the extensive zeolite family of tetrahedral silica frameworks. Since α-quartz can occur naturally as large single crystals and crystallizes in a non-centrosymmetric space group, this also makes it an ideal system for the measurement of elastic and piezoelectric constant tensors.

Here we have used pGFN-FF to optimize the α-quartz structure and compute the curvature related properties using analytic second derivatives, as implemented in this work. Results for the properties of α-quartz are given in Table 4, along with a comparison to a widely used formal charge shell model potential.[64] Properties from experiment and quantum mechanical calculations at the hybrid functional level are also included. Both force field approaches, underestimate the lattice parameters of α-quartz, while the density functional result slightly overestimates them. However, the error from pGFN-FF in the *c* lattice parameter is the most substantial structural discrepancy at almost 4%, which is larger than any difference due to thermal expansion effects. Despite this contraction, the on-diagonal elastic constants are all substantially underestimated, while the quantum mechanical results, and to a lesser extent the shell model, do much better. It should be noted that the latter model was fitted to α-quartz and so it is unsurprising that it is more accurate for this system. Part of the softer mechanical response of pGFN-FF can be attributed to the electrostatics as the partial charge on Si is ~+1.1, which is lower than most force field charges used for this system.

Table 4. Hexagonal lattice parameters (a and c in Å), elastic constants (C_{ij} in GPa), and piezoelectric constants (e_{ij} in C/m²) for α-quartz. Experimental values are from Antao *et al*.[65], Heyliger *et al*.[66], and Tarumi *et al*.,[68] respectively. Quantum mechanical data (B3LYP) are from Harb *et al*.[67]

Property	Expt.	Calc.		
		GFN-FF	B3LYP	Shell model
Lattice parameters				
a	4.913	4.820	4.976	4.836
c	5.405	5.202	5.487	5.346
Elastic constants				
C_{11}	87.3	56.2	89.7	94.6
C_{33}	105.8	74.5	112.0	116.1
C_{44}	57.2	31.2	57.9	50.0
C_{66}	40.4	16.0	38.5	38.1
C_{12}	6.6	24.3	12.8	18.4
C_{13}	12.0	8.2	16.4	19.7
C_{14}	-17.2	-4.0	-14.8	-14.5
Piezoelectric constants				
e_{11}	0.149	0.770	0.184	2.690
e_{14}	-0.057	-0.301	-0.055	-1.403

Piezoelectric strain constants for α-quartz are also given in Table 4. The agreement between the quantum mechanical data and experiment appears to be particularly good. However, the experimental data are for close-to room temperature, whereas the computed values are not. Given that piezoelectric strain constants are found to decrease substantially as the temperature is lowered,[68] the agreement between these values is likely to be fortuitous. On the other hand, despite the piezoelectric constants computed by pGFN-FF being several times larger than experiment, they at least represent an improvement on the shell model values for this system, although we note that a similarly constructed shell model has been found to accurately reproduce the same properties for the closely-related berlinite ($AlPO_4$) structure.[69] Thus it is likely that the error obtained when using the shell model for α-quartz could have been minimized further had the fitting set included reference data for these strain constants.

As noted for previous examples, care must be taken when using pGFN-FF to consider the relative thermodynamics of different structures. An illustration for the case of silica comes from comparison of α-quartz, the tetrahedral stable phase at ambient conditions, with stishovite, which is the high-pressure octahedral form. If naively computed, pGFN-FF would suggest that stishovite is more stable at 0 GPa by over 700 kJ/mol. Of course, this comparison cannot be made since both phases are described with different models generated specifically for the local coordination environment. However, pGFN-FF can be usefully applied to polymorphism of silica for comparison of α-quartz to nanoporous zeolite structures. Here the force field correctly predicts that α-quartz is the ground state based on comparison with all of the zeolites we have tested.

For a second mineral example, let us briefly consider the case of aluminium hydroxide ($Al(OH)_3$), which commonly occurs as the polymorphs gibbsite and bayerite. Both structures are monoclinic and consist of 2D layers that are hydrogen bonded together, while also containing intra-layer hydrogen bonds. Gibbsite and bayerite differ in the interlayer stacking

arrangement, as shown in Figure 6. This system represents a non-trivial system to model accurately with force fields due to the lower symmetry and hydrogen bonding. It was also a somewhat pathological case in that depending on the starting structure the initial charges could be too negative and the calculation has to be aborted due to unphysical parameters.

Figure 6. Interlayer stacking arrangement in the gibbsite and bayerite polymorphs of $Al(OH)_3$. Here oxygen and hydrogen are represented by red and white spheres, respectively, while the octahedra for Al coordination are shown in blue.

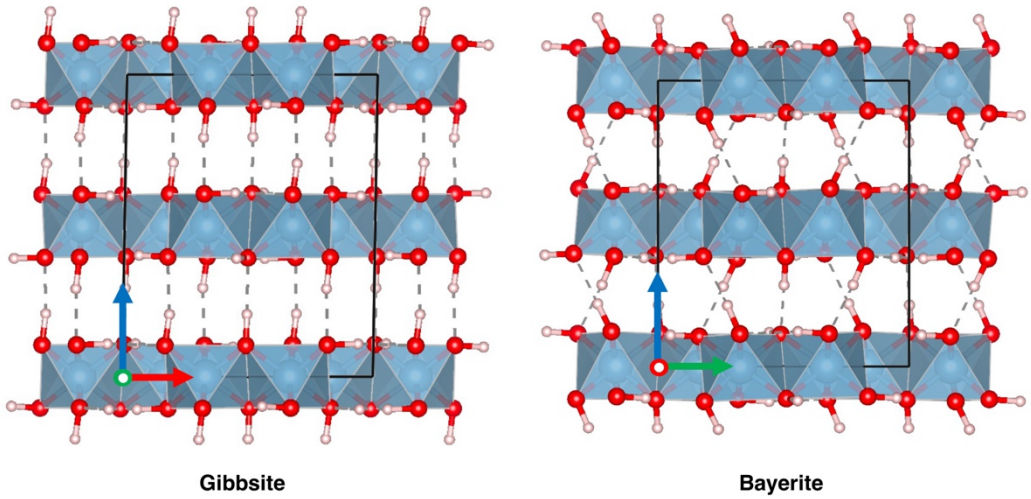

For the case of gibbsite, optimizing starting from the experimental structure leads to low errors in the cell parameters for such a complex system with the largest discrepancy being 2.1% on the *c* axis, which corresponds to the interlayer direction, while the volume and monoclinic angle have errors of only -0.3% and 1.2%, respectively. Analysis of the initial topology finds that this configuration includes some Al-Al bonds, but not for all nearest-neighbor pairs (only two thirds of the possible Al-Al bonds are present). By compressing the initial unit cell slightly it is possible to reach a configuration in which each Al in the structure has three Al-Al bonds. On relaxation, the errors in the lattice parameters now increase to a 5.8% overestimation of the volume, though the difference from experiment lies purely within the layers, as the interlayer direction and monoclinic angle are essentially in perfect agreement to within 0.1%.

For bayerite, the initial configuration used here does not contain Al-Al covalent bonds. Compression of the bayerite structure until Al-Al bonds are formed is found to be problematic,

as only the point where 10 out of the 12 possible bonds can be reached before the initial charges become catastrophically negative. Hence the only way to achieve a meaningful comparison of gibbsite and bayerite as polymorphs is to explicitly exclude Al-Al bonds, even though this leads to larger errors in the structure. Under this constraint, bayerite is found to be the more stable structure by 10.8 kJ/mol, in contrast to the B3LYP internal energy difference of 9.9 kJ/mol in favor of gibbsite,[70] where the latter accords with the sign and approximate magnitude of the experimental free energy difference. Despite both structures having the same topology, the GFN-FF scheme yields slightly different parameters for the angles and torsions between the two structures, which again invalidates the energy comparison. Hence the only way to obtain a valid energy difference would be to use a common reference structure to generate the parameters, which are then applied unchanged to gibbsite and bayerite. Of course, the choice of reference structure may bias the outcome and mapping the equivalent atoms between structures would have to be performed.

Finally for this system, one of the most widely used characterization methods for gibbsite is vibrational spectroscopy. The stretching modes for the OH groups give five distinct peaks in the range of 3373-3620 cm^{-1}, which is in good agreement with quantum mechanical calculations.[71] The computed stretching modes from pGFN-FF are found to occur over a narrower range and at lower frequency (2991-3150 cm^{-1}), pointing to underestimation of the force constants for O-H bonds. This may be because the hydroxyl groups in gibbsite are bridging between two Al atoms, rather than terminal, and so this less common environment may not have formed part of the initial training set.

A further class of minerals is those that contain discrete molecular anions within their structure, such as metal carbonates and sulfates. Here we use these systems as a means to address the best way to describe such minerals within (p)GFN-FF. There are two possible descriptions to examine: The anions (CO_3^{2-}, SO_4^{2-}) could either be covalently bonded to the

cations or treated as discrete species, and in the latter case the fragment is assigned a formal charge of -2. The optimized structures of a range of carbonate and sulfate minerals have been compared against experiment (see Tables S10 and S11).

Examination of the results for a range of carbonate and sulfate minerals show that the accuracy of the structures can vary substantially with the choices made with no single approach proving to be universally the best. However, some general trends can be observed. Firstly, the description of these minerals tends to be most reliable when treating the systems as a covalent framework (i.e., the metal cations are bonded to the oxyanions). If the minerals are described as being composed of non-bonded metals and molecular anions (see Tables S12 and S13), then improved results are obtained by specifying formal charges on the fragments, rather than leaving them to be neutral as they would be by default, though the errors can still be large. Secondly, use of the Wolf sum for the topological charges leads to fewer failures in the calculations when starting from the experimental structures. The source of such failures is usually the initial charges being too negative, such that the repulsive parameters become imaginary. Results after including the Wolf sum also show lower mean absolute errors for the minerals when treated as covalent frameworks. Thirdly, damping of the three-body dispersion often only has a small effect, with the notable exception of barite where the unit cell is remarkably improved. Overall, the results for the carbonate and sulfate minerals indicate that it is best to treat these systems as framework materials within the pGFN-FF formalism.

3.6. Liquid water

So far, the focus has been on application of (p)GFN-FF to the solid-state. However, the inclusion of periodicity also facilities the study of liquids without the need to study droplets where surface effects can have an influence. Here we examine the performance of the current force field for water as it is one of the most widespread liquids in the environment. It also represents a challenging system to describe accurately, which has resulted in a large multitude

of models[72] from simple atom-centered point charge force fields (rigid or flexible), though to those with multiple interaction centers, multipoles and/or polarizability. Quantum mechanical methods have also been widely used for liquid water, though accurate results potentially require consideration of dispersion, more advanced functionals and treatment of nuclear quantum effects.[73,74] Use of machine learning, trained on high-level methods, may represent a pathway to affordable quality simulations of this system.[75]

Molecular dynamics has been performed for a cubic cell of liquid water containing 520 molecules at 300 K. Simulations have been run in the NPT ensemble with a stochastic barostat and thermostat with constants of 1 ps and 0.5 ps, respectively, and a time step of 1 fs. The simulation was initiated from a configuration that had previously been equilibrated with SPC/Fw water.[76] During the initial phase of the molecular dynamics, a contraction of the unit cell was observed and so the simulation was equilibrated until the volume fluctuated around a constant value. Thereafter, production data was analyzed to determine the structure and dynamical properties of the water model. The total simulation length was approximately 350 ps.

As already noted above, the most obvious characteristic of the description of water by GFN-FF, at ambient conditions, is that the density is substantially overestimated at 1.23 g/cm^3. Further insight can be obtained by considering the radial distribution functions, as well as information on the angular correlations, shown in Figure 7. Taken overall, these plots indicate that while GFN-FF gives reasonable local hydrogen-bonding between molecules, the longer-range structure and ordering of molecules deviates strongly from that expected. In particular, the O-O-O angular distribution for neighboring water molecules is essentially flat across a wide range of angles, instead of exhibiting a peak around the tetrahedral angle. This is a consequence of a particular broad distribution of water molecules in the first solvation shell which leads to an approximate number of neighbors of 10.5, in contrast to 4.4 for SPC/Fw.

Figure 7. Comparison of the radial distribution functions for O-H (top left) and O-O (top right) as computed for liquid water at room temperature and pressure using GFN-FF and SPC/Fw water. Experimental data are also included for comparison. For the O-O plot, the integral of the curves are also given (right-hand side y-axis). Probability curves for angular distributions are also given (lower panels) from the two computational models.

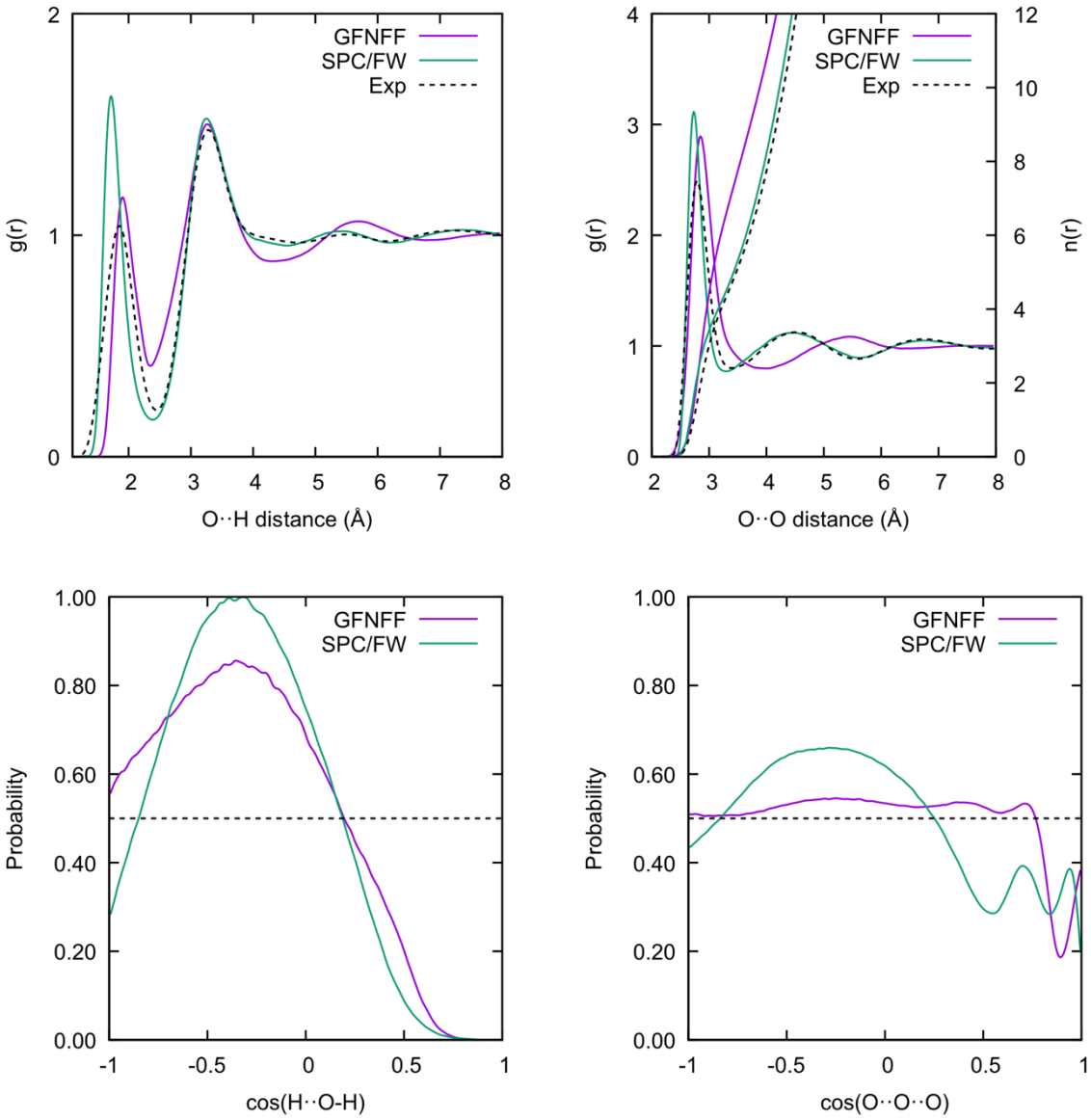

Given the increase in density and large coordination number of water molecules, it is important to ascertain whether the water is freezing or not, as the timescale for homogeneous nucleation of a new phase can be long and depend on the periodic boundary conditions imposed, especially as this has been a problem for previous water models.[77] To check this, a further simulation was performed in which a slab of ice IX was created in 3D boundary conditions with a ~20 Å vacuum gap between layers. This was then simulated using similar parameters to the box of liquid water in an isotropic NPT ensemble, which prevents immediate collapse of the vacuum gap while allowing relaxation in all directions. Inclusion of a surface allows heterogeneous nucleation of melting to occur, and indeed the system rapidly reverts to the liquid phase.

Finally, an important property of liquid water is the self-diffusion coefficient. This is computed with GFN-FF to be 2.06 x 10^{-5} cm^2/s for the current cell size, which is in surprisingly good agreement with the experimental value of 2.35 x 10^{-5} cm^2/s,[78] despite the overestimated density and distinct local structure. Since the self-diffusion coefficient is dependent on the size of the simulation cell used,[79] the present computed value is an underestimate of the converged GFN-FF value, and so extrapolation to the infinite cell limit is likely to lead to even better (fortuitous) agreement with experiment based on the corresponding correction for SPC/Fw water.[80]

4. CONCLUSIONS

In this study, we have described the extension of the universal GFN-FF force field from molecules and clusters to periodic systems. A few changes are mandated by the use of periodic boundary conditions, such as the introduction of Ewald or Parry sums for electrostatics, the sampling of the Brillouin zone for the calculation of the electronic structure of π systems, and the inclusion of strain derivatives to allow for optimization of the lattice vectors. However, a

number of areas for further modification were identified that are beneficial for extended materials, but also lead to changes in the results for finite systems and so the present force field is denoted pGFN-FF to indicate this deviation from the original method. Here the use of a small "p" is intended to indicate the motivation of periodic systems for the changes and the case to recognize that we do not wish to detract from the initial creation of GFN-FF as being the major contribution. Specifically, the main adjustments to the method proposed include the use of damped three-body dispersion to prevent collapse of structures in a small number of cases, and the use of the Wolf sum to screen the electrostatic interactions in the long-range limit during the determination of topological charges in preference to a hard cut-off for the Coulomb term. In addition, the calculation of analytic second derivatives with respect to Cartesian coordinates and/or strain variables has been formulated and implemented.

We have examined the application of the original GFN-FF method, where possible, *vs* the current recommended modified form for a range of types of solid materials from organic molecular crystals through to close-packed ionic solids, layered materials and minerals. Where comparison is possible, we find the pGFN-FF form only leads to small changes in the resulting structures and thermodynamics at the benefit of increased robustness. There is no clear overall trend suggesting either a systematic improvement or deterioration, where the latter might be expected given that the parameters were fitted based on the original GFN-FF formulation.

GFN-FF aims to be a universal force field and is indeed a major advance in terms of useability relative to previous models in this category, as there is no requirement for atom typing or separate determination of atomic charges. However, there are some important issues for someone working with the force field to consider and, where required, control. In particular, the initial geometry defines the bonding topology of the system, from which the parameters follow. Depending on the initial density or configuration chosen then the results may vary. Therefore, it is important to analyze the nature of the initial topology and check the assignment

of fragments before performing extensive calculations. It also comes with the caveat, that while it is universal (at least up for elements up to radon), it isn't reactive; dissociation is allowed, but bonds are not formed by changing the topology on the fly. This means that care is required as to the intended usage. For relaxation of structures and determination of harmonic properties, such as elastic constants and vibrational frequencies, (p)GFN-FF is well-suited in most cases. For defect energies or determining the relative thermodynamics of different structures, such as polymorphism, then this approach will only be applicable for systems with molecular fragments such that no bonding changes are required during the process under examination. Extension of the GFN-FF approach to encompass reactivity should be possible in future though, as has been demonstrated for the universal force field for the case of the IM-UFF variant:[81] Here weighting of atom and bond types is introduced to allow smooth transitions to occur between existing non-reactive interactions. The same effect could also be achieved by empirical valence bond theory or its multi-state variant.[82]

Considering the overall performance of pGFN-FF for solids, we have found that it represents an improvement over UFF for the materials tested (with the possible exception of the interlayer lattice parameter of 2-D hexagonal materials) regardless of whether QEq charges are included or not in the latter method. It is even comparable in accuracy to specifically parameterized variants of UFF for the case of metal-organic frameworks. Organic molecular crystalline solids are found to be overbound, with lattice energies being too exothermic and unit cell volumes too small. Despite this, the average errors are often within a factor of two of those for more sophisticated force fields with complex electrostatic descriptions, which reflects the use of a contemporary dispersion model for these relatively weakly bound systems. The trend toward overbinding of molecular systems is also apparent for liquid water, which exhibits a density that is too high at ambient conditions. One of the reasons why GFN-FF may have systematic errors in intermolecular interactions is because of the limited data available for fitting when

restricted to molecules alone, especially from experiment. By extending the formalism to periodic systems, this opens up the potential to fit to a wide range of crystallographic, mechanical and thermochemical data in future that could lead to improvements in the intermolecular parameters.

In the present study we have demonstrated the application of pGFN-FF to both lattice dynamics and molecular dynamics. While not explicitly considered here, the extension to Monte Carlo simulation is straightforward for ensembles where the number of particles is fixed. The case of Grand Canonical Monte Carlo is more complex as the full topology is no longer defined by the initial structure and will vary throughout the simulation. Provided the species being inserted/removed is restricted to one that has only non-bonded interactions with the rest of the system, as is typically the case, then this future extension would also be feasible.

In conclusion, the extension of GFN-FF to periodic systems provides a valuable new tool for rapid simulation of materials. The automatic assignment of charges and atom types makes the method easy to use and ideal for large-scale screening of systems with minimal user intervention. It also has other potential applications, such as to aid more costly quantum mechanical techniques through providing initial Hessian matrices to accelerate geometry optimization. As with any universal force field, it is unlikely to represent the most accurate answer, but provides a valuable first insight into trends and properties.

ASSOCIATED CONTENT

Supporting Information

Full details of structures and properties for systems studied, the influence of the dispersion drop tolerance on computational cost, and charges used in UFF calculations. Figures S1-9 and Tables S1-13. This information is available free of charge via the Internet at http:pubs.acs.org.

AUTHOR INFORMATION

Corresponding Author

E-mail: J.Gale@curtin.edu.au

Notes

The authors declare no competing financial interest.

Acknowledgements

The Australian Research Council is acknowledged for funding under grant FL180100087, as well as the Pawsey Supercomputing Centre and National Computational Infrastructure for provision of computational resources. Prof. Stefan Grimme is thanked for valuable discussions.

Table of Contents Graphic

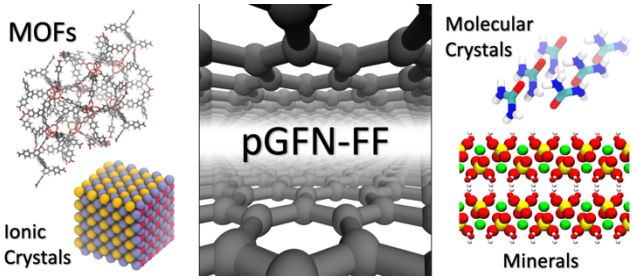

References

[1] Mayo, S.L.; Olafson, B.D.; Goddard III, W.A. DREIDING: A generic force field for molecular simulations. *J. Am. Chem. Soc.* **1990**, *94*, 8897-8909.

[2] Maple, J.R.; Dinur, U.; Hagler, A.T. Derivation of force fields for molecular mechanics and dynamics from *ab initio* energy surfaces. *Proc. Natl. Acad. Sci. USA* **1988**, *85*, 5350-5354.

[3] Rappé, A.K.; Casewit, C.J.; Colwell, K.S.; Goddard III, W.A.; Skiff, W.M. UFF, a full periodic table force field for molecular mechanics and molecular dynamics simulations. *J. Am. Chem. Soc.*, **1992**, *114*, 10024-10035.

[4] Addicoat, M.A., Vankova, N., Akter, I.F. & Heine, T. Extension of the universal force field to metal–organic frameworks. *J. Chem. Theory Comput.* **2014***, 10*, 880-891.

[5] Ogawa, T.; Nakano, T. The extended universal force field (XUFF): Theory and applications. *Chem-Bio Inf. J.*, **2010**, *10*, 111-133.

[6] Rappé, A.K.; Goddard III, W.A. Charge equilibration for molecular dynamics simulations. *J. Phys. Chem.* **1991**, *95*, 3358-3363.

[7] Unke, O.T.; Chmiela, S.; Sauceda, H.E.; Gastegger, M.; Poltavsky, I.; Schutt, K.T.; Tkatchenko, A.; Muller, K.-R. Machine learning force fields. *Chem. Rev.* **2021**, *121*, 10142-10186.

[8] Spicher, S.; Grimme, S. Robust atomistic modeling of materials, organometallic, and biochemical systems. *Angew. Chem., Intl. Ed.* **2020**, *59*, 15665-15673.

[9] https://github.com/grimme-lab/xtb

[10] Catlow, C.R.A.; Mackrodt, W.C. Theory of simulation methods for lattice and defect energy calculations in crystals. *Lecture Notes Phys*. **1982,** *166*, 1-20.

[11] Mortier, W.J.; Ghosh, S.K.; Shankar, S. Electronegativity-equalization method for the calculation of atomic charges in molecules. *J. Am. Chem. Soc.* **1986**, *108*, 4315-4320.

[12] Ewald, P.P. Die Berechnung optischer und elektrostatischer Gitter potentiale. *Ann. Phys.* **1921**, *369*, 253-287.

[13] Parry, D.E. The electrostatic potential in the surface region of an ionic crystal. *Surf. Sci.* **1975**, *49*, 433-440.

[14] Saunders, V.R.; Freyia-Fava, C.; Dovesi, R.; Roetti, C. On the electrostatic potential in linear periodic polymers. *Comp. Phys. Commun.* **1994**, *84*, 156-172.

[15] Nakano, A. Parallel preconditioned conjugate-gradient approach to variable-charge molecular dynamics. *Comp. Phys. Commun.* **1997**, *104*, 59-69.

[16] Wolf, D.; Keblinski, P.; Philpot, S.R.; Eggebrecht, J. Exact method for the simulation of Coulombic systems by spherically truncated, pairwise r^{-1} summation. *J. Chem. Phys.* **1999**, *110*, 8254-8282.

[17] Fennell, C.J.; Gezelter, J.D. Is the Ewald summation still necessary? Pairwise alternatives to the accepted standard for long-range electrostatics. *J. Chem. Phys.* **2006**, *124*, 234104.

[18] Monkhorst, H.J.; Pack, J.D. Special points for Brillouin-zone integrations. *Phys. Rev. B* **1976**, *13*, 5188-5192.

[19] Mei, J.; Davenport, J.W.; Fernando, G.W. Analytic embedded-atom potentials for fcc metals: Application to liquid and solid copper. *Phys. Rev. B* **1991**, *43*, 4653-4658.

[20] Caldeweyher, E.; Ehlert, S.; Hansen, A.; Neugebauer, H.; Spicher, S.; Bannwarth, C.; Grimme, S. A generally applicable atomic-charge dependent London dispersion correction. *J. Chem. Phys.* **2019**, *150*, 154122.

[21] Otero-de-la-Roza, A.; Johnson, E.R. Many-body dispersion interactions from the exchange-hole dipole moment model. *J. Chem. Phys.* **2013**, *138*, 054103.

[22] Proynov, E.; Liu, F.; Gan, Z.; Wang, M.; Kong, J. Density-functional approach to the three-body dispersion interaction based on the exchange dipole moment. *J. Chem. Phys.* **2015**, *143*, 084125.

[23] Becke, A.D.; Johnson, E.R. A density-functional model of the dispersion interaction. *J. Chem. Phys.* **2005**, *123*, 154101.

[24] Sato, T.; Tsuneda, T.; Hirao, K. Van der Waals interactions studied by density functional theory. *Mol. Phys.* **2005**, *103*, 1151-1164.

[25] Gale, J.D.; Rohl, A.L. The General Utility Lattice Program (GULP). *Mol. Simul.* **2003**, *29*, 291-341.

[26] Otero-de-la-Roza, A.; Johnson, E.R. A benchmark for non-covalent interactions in solids. *J. Chem. Phys.* **2012**, *137*, 054103.

[27] Reilly, A.M.; Tkatchenko, A. Understanding the role of vibrations, exact exchange, and many-body van der Waals interactions in the cohesive properties of molecular crystals. *J. Chem. Phys.* **2013**, *139*, 024705.

[28] Dolgonos, G.A.; Hoja, J.; Boese, A.D. Revised values for the X23 benchmark set of molecular crystals. *Phys. Chem. Chem. Phys.* **2019**, *21*, 24333-24344.

[29] Buchholz, H.K.; Stein, M. Accurate lattice energies of organic molecular crystals from periodic Turbomole calculations. J. Comput. Chem. 2018, 39, 1335-1343.

[30] Thomas, S.P.; Spackman, P.R.; Jayatilaka, D.; Spackman, M.A. Accurate lattice energies for molecular crystals from experimental crystal structures. *J. Chem. Theory Comput.* **2018**, *14*, 1614-1623.

[31] Coombes, D.S.; Price, S.L.; Willock, D.J.; Leslie, M. Role of electrostatic interactions in determining the crystal structures of polar organic molecules. A distributed multipole study. *J. Phys. Chem.* **1996**, *18*, 7352-7360.

[32] Nyman, J.; Pundyke, O.S.; Day, G.M. Accurate force fields and methods for modelling organic molecular crystals at finite temperatures. *Phys. Chem. Chem. Phys.* **2016**, *18*, 15828-15837.

[33] Tao, J.; Zheng, F.; Gebhardt, J.; Perdew, J.P.; Rappe, A.M. Screened van der Waals correction to density functional theory for solids. *Phys. Rev. Mater*. **2017**, *1*, 020802(R).

[34] Nepal, N.K.; Ruzsinszky, A. Rock salt or cesium chloride: Investigating the relative stability of the cesium halide structures with random phase approximation based methods. *Phys. Rev. B* **2018**, *97*, 115140.

[35] Otero-de-la-Roza, A.; Johnson, E.R. Application of XDM to ionic solids: The importance of dispersion for bulk moduli and crystal geometries. *J. Chem. Phys*. **2020**, *153*, 054121.

[36] Scheiber, H.O.; Patey, G.N. Analysis of the relative stability of lithium halide crystal structures: Density functional theory and classical models. *J. Chem. Phys*. **2021**, *154*, 184507.

[37] Joung, I.S; Cheatham III, T.E. Determination of alkali and halide monovalent ion parameters for use in explicitly solvated biomolecular simulations. *J. Phys. Chem. B* **2008**, *112*, 9020-9041.

[38] Wright, K.; Gale, J.D. Interatomic potentials for the simulation of the zinc-blended and wurtzite forms of ZnS and CdS: Bulk structure, properties, and phase stability. *Phys. Rev. B* **2004**, *70*, 035211.

[39] Jain, A.; Ong, S.P.; Hautier, G.; Chen, W.; Richards, W.D.; Dacek, S.; Cholia, S.; Gunter, D.; Skinner, D.; Ceder, G.; Persson, K.A. The Materials Project: A materials genome approach to accelerating materials innovation. *APL Materials* **2013**, *1*, 011002.

[40] Slater, J.C. Atomic Radii in Crystals. *J. Chem. Phys*. **1964**, *41*, 3199-3204.

[41] Gutierrez, H.R. Two-dimensional layered materials offering expanded applications in flatland. *ACS Appl. Nano. Mater.* **2020**, *3*, 6134-6139.

[42] Geim, A.K.; Grigorieva, I.V. Van der Waals heterostructures. *Nature* **2013**, *499*, 419-425.

[43] Rasmussen, F.A.; Thygsens, K.S. Computational 2D materials database: Electronic structure of transition-metal dichalcogenides and oxides. *J. Phys. Chem. C* **2015**, *119*, 13169-13183.

[44] Acharyya, P.; Kundu, K.; Biswas, K. 2D layered all-inorganic halide perovskites: recent trends in their structure, synthesis and properties. *Nanoscale* **2020**, *12*, 21094-21117.

[45] Yan, J.; Qiu, W.; Wu, G.; Heremans, P.; Chen, H. Recent progress in 2D/quasi-2D layered metal halide perovskites for solar cells. *J. Mater. Chem. A* **2018**, *6*, 11063-11077.

[46] Kim, C.; Huan, T.D.; Krishnan, S.; Ramprasad, R. Data descriptor: A hybrid organic-inorganic perovskite dataset. *Sci. Data* **2017**, *4*, 170057.

[47] Mao, L.; Stoumpos, C.C.; Kantzidis, M.G. Two-dimensional hybrid halide perovskites: Principles and promises. *J. Am. Chem. Soc*. **2019**, *141*, 1171-1190.

[48] Marchenko, E.I.; Fateev, S.A.; Petrov, A.A.; Korolev, V.V.; Mitrofanov, A.; Petrov, A.V.; Goodilin, E.A.; Tarasov, A.B. Database of two-dimensional hybrid perovskite materials: Open-access collection of crystal structures, band gaps, and atomic partial charges predicted by machine learning. *Chem. Mater*. **2020**, *32*, 7383-7388.

[49] Correa-Baena, J.P.; Saliba, M.; Buonassisi, Grätzel, M.; Abate, A.; Tress, W.; Hagfeldt, A. Promises and challenges of perovskite solar cells. *Science* **2017**, *358*, 739-744.

[50] Zheng, K.; Pullerits, T. Two dimensions are better for perovskites. *J. Phys. Chem. Lett*. **2019**, *10*, 5881-5885.

[51] Björkman, T.; Gulans, A.; Krasheninnikov, A.V.; Nieminen, R.M. van der Waals bonding in layered compounds from advanced density-functional first-principles calculations. *Phys. Rev. Lett*. **2012**, *108*, 235502.

[52] Björkman, T. Testing several recent van der Waals density functionals for layered structures. *J. Chem. Phys*. **2014**, *141*, 074708.

[53] Tawfik, S.A.; Gould, T.; Stampfl, C.; Ford, M.J. Evaluation of van der Waals density functionals for layered materials. *Phys. Rev. Mater*. **2018**, *2*, 034005.

[54] Otero-de-Roza, A.; LeBlanc, L.M.; Johnson, E.R. Asymptotic pairwise dispersion corrections can describe layered materials accurately. *J. Phys. Chem. Lett.* **2020**, *11*, 2298-2302.

[55] Seidu, A.; Himanen, L.; Li, J.; Rinke, P. Database-driven high-throughput study for hybrid perovskite coating materials. *New J. Phys*. **2019**, *21*, 083018.

[56] Zhao, J.; Deng, Y.; Wei, H.; Zheng, X.; Yu, Z.; Shao, Y.; Shield, J.E; Huang, J. Strained hybrid perovskite thin films and their impact on the intrinsic stability of perovskite solar cells. *Sci. Adv.* **2017**, *3*, eaao5616.

[57] Wu, J.; Liu, S.-C.; Li, Z.; Wang, S.; Xue, D.-J.; Lin, Y.; Hu, J.-S. Strain in perovskite solar cells: origins, impacts and regulation. *Nat. Sci. Rev*. **2021**, *0*, nwab047.

[58] Wang, L.; Chen, P.; Kuttipillai, P.S.; King, I.; Staples, R.; Sun, K.; Lunt, R.R. Epitaxial stabilization of tetragonal cesium tin iodide. *ACS Appl. Mater. Interfaces* **2019**, *11*, 32076-32083.

[59] Kim, H.-S.; Park, N.-G. Importance of tailoring lattice strain in halide perovskite crystals. *NPG Asia Materials* **2020**, *12*, 78.

[60] Kepenekian, M.; Traore, B.; Blancon, J.-C.; Pedesseau, L.; Tsai, H.; Nie, W.; Stoumpos, C.C.; Kanatzadis, M.G.; Even, J.; Mohite, A.D.; Tretiak, S.; Katan, C. Concept of lattice mismatch and emergence of surface states in two-dimensional hybrid perovskite quantum wells. *Nano Lett*. **2018**, *18*, 5603-5609.

[61] Rathnayake, P.V.G.M.; Bernardi, S.; Widmer-Cooper, A. Evaluation of the AMOEBA force field for simulating metal halide perovskites in the solid state and in solution. *J. Chem. Phys.* **2020**, *152*, 024117.

[62] Chung, Y.G.; Haldoupis, E.; Bucior, B.J.; Haranczyk, M.; Lee, S.; Vogiatzis, K.D.; Milisavljevic, M.; Ling, S.; Camp, J.S., Slater, B., Siepmann, J.I.; Sholl, D.S.; Snurr, R.Q. Advances, updates, and analytics for the Computation-Ready Experimental Metal-Organic Framework Database: CoRE MOF 2019. *J. Chem. Eng. Data* **2019**, *64*, 5985-5998.

[63] http://aam.ceb.cam.ac.uk/mof-explorer

[64] Sanders, M.J.; Leslie, M.; Catlow, C.R.A. Interatomic potentials for SiO_2. *J. Chem. Soc., Chem. Commun.* **1984**, 1271-1273.

[65] Antao, S.M.; Hassan, I.; Wang, J.; Lee, P.L.; Toby, B.H. State-of-the-art high-resolution powder X-ray diffraction (HRPXRD) illustrated with Rietveld structure refinement of quartz, sodalite, tremolite and meionite. *Can. Miner.* **2008**, *46*, 1501-1509.

[66] Heyliger, P.; Ledbetter, H.; Kim, S. Elastic constants of natural quartz. *J. Acoust. Soc. Am.* **2003**, *114*, 644-650.

[67] Harb, M.; Labéguerie, P.; Baraille, I.; Rérat, M. Response of low quartz SiO_2 to the presence of an external static electric field: A density functional theory study. *Phys. Rev. B* **2009**, *80*, 235131.

[68] Tarumi, R.; Nakamura, K.; Ogi, H.; Hirao, M. Complete set of elastic and piezoelectric coefficients of α-quartz at low temperatures. *J. Appl. Phys.* **2007**, *102*, 113508.

[69] Gale, J.D.; Henson, N.J. Derivation of interatomic potentials for microporous aluminophosphates from the structure and properties of berlinite. *J. Chem. Soc. Faraday Trans.* **1994**, *90*, 3175-3179.

[70] Demichelis, R.; Civalleri, B.; Noel, Y.; Meyer, A.; Dovesi, R. Structure and stability of aluminium trihydroxides bayerite and gibbsite: A quantum mechanical *ab initio* study with the Crystal06 code. *Chem. Phys. Lett.* **2008**, *465*, 220-225.

[71] Balan, E.; Lazzeri, M.; Morin, G.; Mauri, F. First-principles study of the OH-stretching modes of gibbsite. *Am. Miner.* **2006**, *91*, 115-119.

[72] Guillot, B. A reappraisal of what we have learnt during three decades of computer simulations on water. *J. Mol. Liquid* **2002**, *101*, 219-260.

[73] Gillan, M.J.; Alfè, D.; Michaelides, A. Perspective: How good is DFT for water? *J. Chem. Phys.* **2016**, *144*, 130901.

[74] Ceriotti, M.; Fang, W.; Kusalik, P.G.; McKenzie, R.H.; Michaelides, A.; Morales, M.A.; Markland, T.E. Nuclear quantum effects in water and aqueous systems: Experiment, theory, and current challenges. *Chem. Rev.* **2016**, *116*, 7529-7550.

[75] Cheng, B.; Engel, E.A.; Behler, J.; Dellago, C.; Ceriotti, M. Ab initio thermodynamics of liquid and solid water. *Proc. Natl. Acad. Sci. USA* **2019**, *116*, 1110-1115.

[76] Wu, Y.; Tepper, H.; Voth, G.A. Flexible simple point-charge water model with improved liquid-state properties. *J. Chem. Phys*. **2006**, *124*, 024503.

[77] Van Maaren, P.J.; van der Spoel, D. Molecular dynamics simulations of water with novel shell-model potentials. *J. Phys. Chem. B* **2001**, *105*, 2618.

[78] Kell, G.S. Precise representation of volume properties of water at one atmosphere. *J. Chem. Eng. Data* **1967**, *12*, 66-69.

[79] Yeh, I.; Hummer, G. System-size dependence of diffusion coefficients and viscosities from molecular dynamics simulations with periodic boundary conditions. *J. Phys. Chem. B* **2004**, *108*, 15873-15879.

[80] Raiteri, P.; Demichelis, R.; Gale J.D. Thermodynamically consistent force field for molecular dynamics simulations of alkaline-earth carbonates and their aqueous speciation. *J. Phys. Chem. C* **2015**, *119*, 24447-24458.

[81] Jaillet, L.; Artemova, S.; Redon, S. IM-UFF: Extending the universal force field for interactive molecular modelling. *J. Mol. Graph. Model.* **2017**, *77*, 350-362.

[82] Schmitt, U.W.; Voth, G.A. Multistate empirical valence bond model for proton transport in water. *J. Phys. Chem. B* **1998**, *102*, 5547-5551.